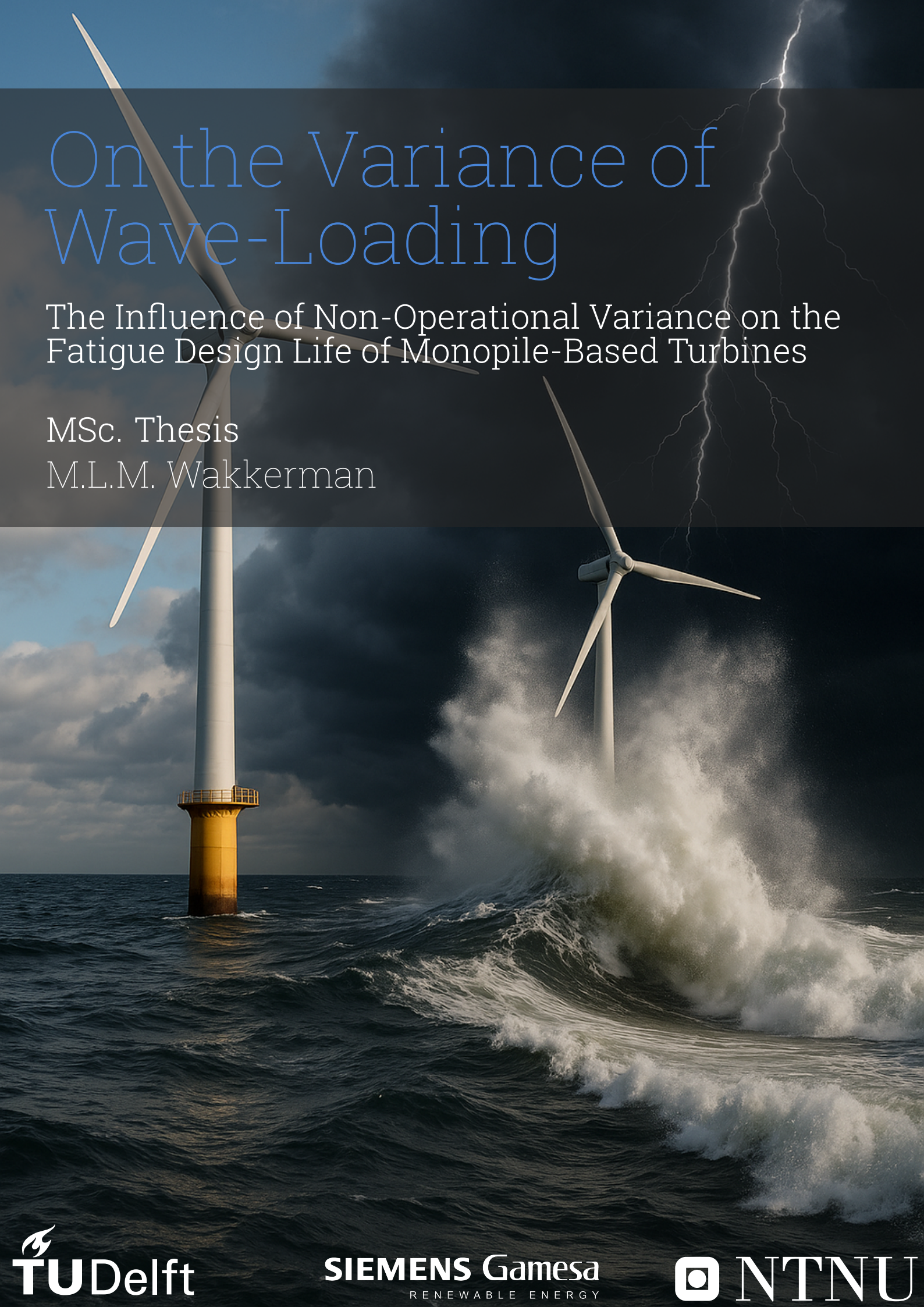

On the Variance of Wave-Loading

The Influence of Non-Operational Variance on the Fatigue Design Life of Monopile-Based Turbines

MSc. Thesis

M.L.M. Wakkerman

TU Delft
SIEMENS Gamesa RENEWABLE ENERGY
NTNU

On the Variance of Wave-Loading

The Influence of Non-Operational Variance on the Fatigue Design Life of Monopile-Based Turbines

by

M.L.M. Wakkerman

To obtain the degree of Master of Science in:
Offshore and Dredging Engineering of Delft University of Technology
&
Technology in Wind Energy of the Norwegian University of Science and Technology

To be defended publicly on 9 of October 2025, at 13.00.

Student number at TU Delft:	5111544	
Student number at NTNU:	123742	
Project Duration:	February, 2025 - October, 2025	
Thesis committee:	Professor M. Muskulus	NTNU, supervisor
	Dr. Ir. P.C. Meijers	TU Delft, supervisor
	Dr. Ir. P. van der Male	TU Delft, supervisor
	Ir. N. Maljaars	Siemens Gamesa, supervisor

Cover: Artificially generated picture using ChatGPT

An electronic version of this thesis is available at http://repository.tudelft.nl/

TU Delft SIEMENS Gamesa RENEWABLE ENERGY NTNU

Preface

This thesis is submitted in fulfillment of the requirements for the offshore engineering track of the European Wind Energy Master at TU Delft and the Norwegian University of Science and Technology (NTNU). The work was carried out at Siemens Gamesa Renewable Energy between February 2025 and August 2025.

I would like to thank my company supervisor, Nico Maljaars, for providing consistent support throughout the project. As my first experience within my field of study, it was a steep learning curve, and your practical advice helped me grow both technically and professionally. I gained a lot from your feedback and will carry a lot of your lessons forward in the next steps of my career.

I also want to thank Michiel van der Meulen, especially for all wave- and software-related questions and his endless interest in the topic of the thesis, and Marc Seidel for his input and for helping to shape the project in a meaningful way.

I appreciate the guidance and feedback from my academic supervisors at TU Delft and NTNU. At TU Delft, I would like to thank Dr. Peter Meijers and Dr. Pim van der Male for their valuable feedback throughout the process.

At NTNU, I'm thankful to my supervisor, Professor Michael Muskulus. You challenged me with difficult questions, offered just enough of a hint when I was stuck, and patiently guided me back to the point where I did understand, a method that pushed me to think hard and develop a stronger grasp of the material.

Thanks also to the Siemens Gamesa colleagues and the group of interns for contributing to a productive, engaging and fun work environment.

Finally, I want to thank my girlfriend, parents and friends, for their support during this period.

Matthijs Wakkerman
The Hague, October 2025

Abstract

The size of offshore wind turbines has increased rapidly in the last decade. This growth has altered the dynamic response of monopile-based support structures, making them more sensitive to wave-induced loading during periods of low aerodynamic damping. Current design standards, such as IEC-61400, estimate fatigue damage using long-term hindcasts, where the mean fatigue damage is calculated over all possible non-operational periods. While this provides a standardised basis for fatigue estimation, it risks under-representing the impact of fatigue-critical sea states occurring during low-damping conditions.

This thesis investigates how variance in wave-induced response loading, driven by variances in availability, influences the fatigue life of monopile-based offshore wind turbines. SCADA availability data from an 8 MW wind farm is used to estimate turbine availability patterns. An existing availability model, based on a Markov process, was adapted to be SCADA-driven. Combined with frequency-domain simulations, this approach demonstrates how variance in availability influences fatigue damage predictions. The framework is applied to both an 8 MW and a 14 MW turbine to assess fatigue sensitivity to availability variances across different turbine sizes.

Several hyperparameters emerged when the original availability model was adapted. To investigate this, multiple model configurations were tested. The SCADA dataset was divided into training and test sets. Transition probabilities between operational and non-operational states were estimated from the training set, and the test set was used to evaluate the different configurations. The final model was benchmarked against SCADA availability profiles and matched with frequency-domain simulations. Validation showed that the availability model slightly overpredicted mean fatigue damage and variance in four sectors, including the driving sector. In two sectors, it substantially overpredicted both metrics.

The availability model was then applied to predict fatigue damage variance over the full design life of both an 8 MW and a 14 MW turbine. Incorporating availability variance produced only a small variance in fatigue damage. For the 14 MW turbine, however, the model suggested slightly higher fatigue damage than expected under the DNV recommendation, which assumes a conservative 10% non-operational ratio.

Fatigue damage variance in large turbines is influenced by availability, which in turn depends on site-specific variances in metocean conditions. This variance may be further amplified by extreme sea states, whose rarity and severity are projected to change under long-term climate change. this indicates the need for site-specific partial safety factors. Future work should therefore extend availability modelling by coupling it with fatigue limit state evaluation. This should include sampling from longer, more varied hindcasts and metocean datasets. Such improvements would ensure that rare but fatigue-critical sea states are better represented, given their disproportionate impact on fatigue life.

Contents

List of Figures

List of Tables

Abbreviations and Symbols

API Application Programming Interface.

COV Coefficient Of Variation.

DEL Damage Equivalent Load.
DLC Design Load Case.
DNV Det Norske Veritas.

ERA European Centre for Medium-Range Weather Forecasts Reanalysis.

FDF Fatigue Design Factor.
FLS Fatigue Limit State.

IEA International Energy Agency.
IEC International Electrotechnical Commission.
ISO International Organization for Standardization.

JONSWAP Joint North Sea Wave Project Spectrum.

LCOE Levelized Cost Of Energy.

MTTF Mean Time To Failure.
MTTR Mean Time To Repair.

NREL National Renewable Energy Laboratory.

PDF Probability Density Function.
PSF Partial Safety Factor.

RNA Rotor Nacelle Assembly.

SCADA Supervisory Control And Data Acquisition.
SCF Stress Concentration Factor.
SuS Support Structure.

ULS Ultimate Limit State.

Symbols

Regular Symbols

Symbol	Definition	Unit
A	Area	[m^2]
C	Correction factor to calibrate turbine specific availability	[-]
C_D	Drag coefficient	[-]
C_a	Added mass coefficient	[-]
C_p	Power coefficient	[-]
C_m	Inertia coefficient	[-]
D	Fatigue damage	[-]
d	Diameter	[m]
$\bar{d}_i$	Average duration of non-operational period in non-operational class i	[min]
E	Young's modulus	[MPa]
f	Force per unit length	[N/m]
f_1	First bending mode natural frequency	[Hz]
H_s	Significant wave height	[m]
I	Second moment of area	[m^4]
K	Intercept of SN-curve	[MPa]
L_{monopile}	Height of monopile substructure	[m]
L_{tot}	Total height of support structure	[m]
L_{tower}	Height of wind turbine tower	[m]
M_{top}	Weight of RNA	[kg]
m	Wöhler slope	[-]
N_{bin}	Number of non-operational classes used in the availability model	[-]
N_i	Number of cycles to failure at stress range i	[-]
N_{WT}	Number of wind turbines simulated with the availability model	[-]
n_i	Number of cycles experienced at stress range i	[-]
P	Power	[W]
P_f	Probability of failure	[-]
S_i	Number of transitions into non-operational class i	[-]
T_n	Natural period	[s]
T_{op}	Total operational time	[min]
T_p	Peak wave period	[s]
U_{target}	Sampled target unavailability ratio	[-]
U_{sim}	Simulated unavailability ratio	[-]
u	Water velocity	[m/s]
$\dot{u}$	Water acceleration	[m/s^2]
V	Wind speed	[m/s]
$V_{\text{cut-in}}$	Cut-in wind speed of wind turbine	[m/s]
$V_{\text{cut-out}}$	Cut-out wind speed of wind turbine	[m/s]
X_{dyn}	Dynamic model uncertainty	[-]
X_{SCF}	SCF model uncertainty	[-]
X_{wave}	Wave load model uncertainty	[-]
X_{wind}	Wind load model uncertainty	[-]
z	Height	[m]
$1P$	Rotor rotational frequency	[Hz]
$3P$	Blade-passing frequency for a 3-bladed rotor	[Hz]

Greek Symbols

Symbol	Definition	Unit
α	Turbine availability ratio	[-]
α_p	Wind shear power law exponent	[-]
β	Reliability index	[-]
γ	JONSWAP peak enhancement factor	[-]
γ_f	Fatigue load partial safety factor	[-]
γ_m	Material partial safety factor	[-]
Δ	Palmgren-Miner's rule model uncertainty	[-]
$\Delta\sigma$	Stress range	[MPa]
Δt	SCADA data time resolution	[min]
λ_i	Probability of transition from available state to unavailable state for non-operational class i	[-]
$\bar{\lambda}_m$	Mass per unit length of the support structure	[kg/m]
$\lambda_{1,eq}$	Equivalent probability of transition from available to degraded state of the total system	[-]
$\lambda_{1,n}$	Probability of transition from available to degraded state of component n	[-]
$\lambda_{2,n}$	Probability of transition from degraded to unavailable state of component n	[-]
μ_{Dam}	Mean fatigue damage	[-]
μ_{eq}	Equivalent probability of transition from unavailable to available state of the total system	[-]
μ_i	Probability of transition from unavailable state to available state for non-operational class i	[-]
μ_n	Probability of transition from unavailable state to available state of component n	[-]
π_0	Long-term unavailability ratio of turbine	[-]
π_1	Long-term availability ratio of turbine	[-]
ρ	Density	[kg/m^3]
Φ	Standard normal cumulative distribution function	[-]

1

Introduction

This chapter will introduce background information and fundamental concepts used in this thesis. It will give an overview of the developments in the offshore wind industry and also note its challenges. Furthermore, it will define the problem statement and the resulting research objectives and questions. Finally, an outline for the following chapters will be provided.

1.1. The Role of Offshore Wind in the Energy Transition

As technological advancements have driven our ever-growing energy demand, humanity has relied heavily on fossil fuels, emitting vast amounts of greenhouse gases in the process. Although these advancements have significantly improved human health and prosperity, they have also led and will lead to severe environmental consequences [1].

In the 21st century, one of humanity's greatest challenges is mitigating and adapting to climate change and its far-reaching effects. One crucial aspect of this challenge is the transition to sustainable and renewable energy sources. The same technological advancements that contributed to climate change will be essential in developing solutions to combat it.

Offshore wind energy is a typical example of such a solution. In 1991, the first offshore wind farm was built with 11 wind turbines, each producing 450 kW [2]. Today, wind farms consisting of up to 175 wind turbines have been constructed. Wind turbine prototypes exceeding 20,000 kW in power output are built, defying the limits of what was thought to be impossible [3, 4].

The growth of offshore wind energy over the past decade is illustrated in Figure 1.1. This upward trend is projected to continue, with global offshore wind energy power production capacity expected to surpass 520 GW by 2040 [5].

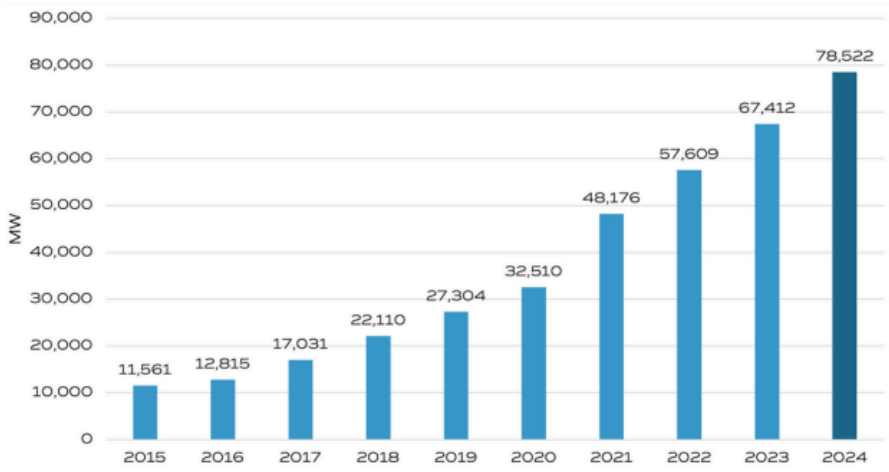

Figure 1.1: Total global offshore wind energy production capacity per year in MW [6].

1.1.1. Fundamentals of Wind Energy

The standard design for modern wind turbines is a three-bladed, upwind (wind-facing) configuration. Wind turbines convert the kinetic energy of moving air into electrical power. As wind flows over the blades, shaped with an airfoil cross-section, a pressure difference is generated between the upper and lower surfaces, producing aerodynamic lift. This lift causes the blades to rotate, which are connected to a shaft inside the nacelle via the hub. The shaft is connected to a generator directly or via a gearbox, which converts the mechanical torque into electrical energy.

1.1.2. Offshore Wind Energy

Installing offshore wind turbines instead of onshore comes with advantages and challenges. The key advantages are the increase in the average wind speed and the consistency of the wind speed compared to onshore wind turbines [7].

The higher average wind speed when moving offshore is illustrated in Figure 1.2. As can be seen in Equation (1.1), the power harvested from a wind turbine is cubically related to the wind speed, V. For example, an increase of the average annual wind speed from 8 to 9 m/s by moving from onshore to offshore could result in a 42% increase in power production.

$$P = \frac{1}{2} C_p A \rho V^3 \tag{1.1}$$

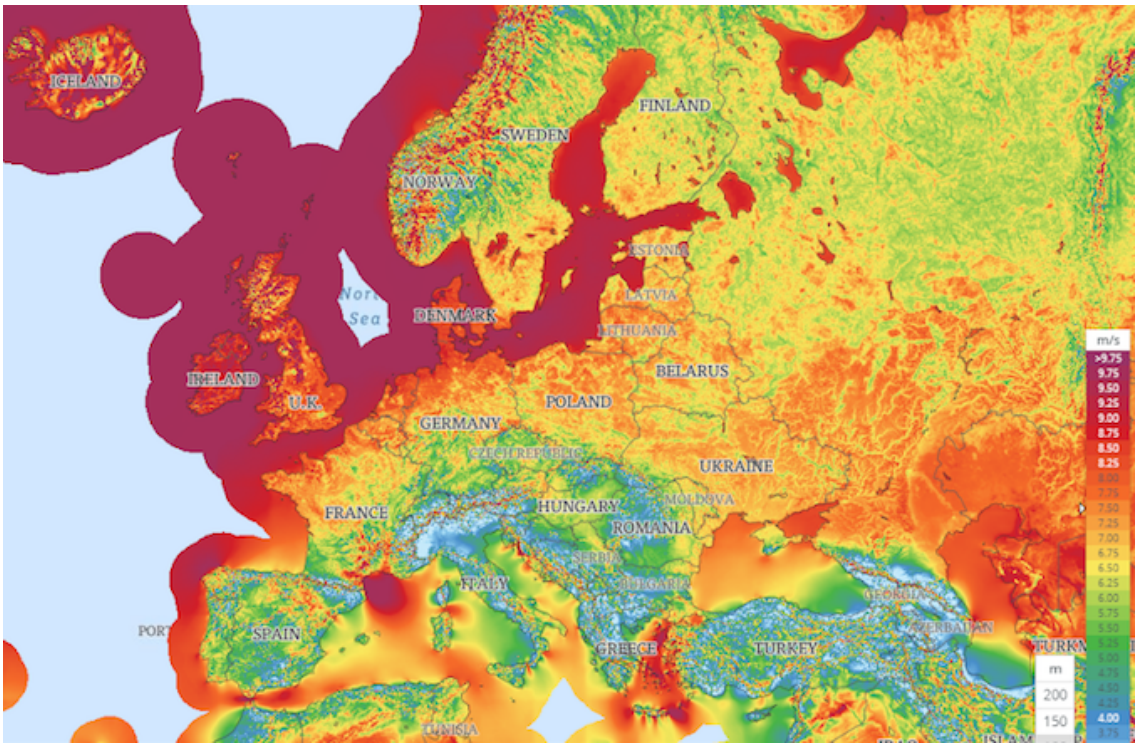

Figure 1.2: Average annual wind speed at 100 m surface elevation across Europe [8].

Another advantage of offshore wind turbines compared to their onshore counterparts is that they do not compete for land use. This makes them an attractive option for regions with a high population density [9]. Furthermore, their distance from residential areas reduces noise pollution and visual impact, making them less intrusive than onshore wind farms [10].
However, offshore wind energy also presents several challenges compared to onshore wind energy. Offshore wind turbines must endure harsher environmental conditions, including higher wind speeds and additional wave loading leading to higher initial investment costs [10].

1.1.3. Advancements in Offshore Wind Energy

To sustain the growth of offshore wind energy, as discussed in Section 1.1, it is essential to ensure that the safety and reliability criteria are met while cost reduction is critical. The cost can be quantitatively assessed using the Levelized Cost Of Energy (LCOE). This metric enables comparison of the cost effectiveness of different energy production technologies by expressing the average cost per unit of electricity generated over a project's lifetime.

Increase in Rotor Size

One key driver for reducing the LCOE of offshore wind energy has been the continuous increase in turbine size, since the energy that a turbine produces is proportional to the swept area of its rotor, as shown in Equation (1.1). The rotor area is given by $A = \pi r^2$, where r is the rotor radius. Thus, increasing the rotor radius by a factor of two results in a fourfold increase in the swept area and, thus, also in power output. This is a clear example of economies of scale, where larger turbines generate more energy at a lower cost per unit of energy [11].

Increase in Height

In addition to capturing more wind, larger turbines are typically taller, allowing access to higher-altitude wind flows, where wind speeds are greater and more consistent. The wind speed at a given height above ground level can be approximated using the wind shear power law, expressed below in Equation (1.2).

$$V(z) = V_{\text{ref}} \left(\frac{z}{z_{\text{ref}}} \right)^{\alpha_p} \tag{1.2}$$

Where $V(z)$ is the wind speed at height z, V_{ref} is the known wind speed at a reference height z_{ref}, and α is the shear exponent, typically ranging from 0.10 over the ocean to 0.3 or higher in rougher terrain onshore.

Example: The National Renewable Energy Laboratory (NREL) 5 MW reference turbine has a hub height of 90 m [12], whereas the International Energy Agency (IEA) 15 MW reference turbine is designed with a hub height of 150 m [13]. Using a power law exponent of $\alpha_p = 0.12$, which is typical for offshore, open sea, environments and recommended by Det Norske Veritas (DNV) [14], the difference in wind speed can be estimated using Equation (1.2):

$$\left(\frac{150}{90} \right)^{0.12} \approx 1.0632$$

This indicates an approximate 6.32% increase in average wind speed due to the increased hub height. Since the power output of a turbine is proportional to the cube of the wind speed, the relative increase in potential power output becomes approximately 20%. This significantly improves the energy yield and economic performance of taller turbines.

Overall Impact of Turbine Size on LCOE

Partly due to the advantages associated with increased turbine size, offshore wind turbines have grown significantly over the past decades. This scale-up has contributed to a substantial reduction in their LCOE, which declined from 218 $/MWh in 2009 to 74 $/MWh in 2023, achieving cost parity with fossil fuel-based generation [15].

However, the increase in the size of offshore wind turbines also requires significantly more steel and rare earth metals, which are costly and energy-intensive to produce [16]. Recent geopolitical tensions, global supply chain disruptions and inflation have driven up energy prices, increasing the cost of materials critical to construct turbines [17]. Moreover, inflation has led to higher interest rates, increasing the cost of capital for offshore wind energy projects and reversing the past downward trend of LCOE. Due to these reasons numerous offshore wind energy projects have been cancelled [18].

These developments underscore the importance of continued research into cost-reduction strategies and material efficiency, while also ensuring that reliability and safety requirements are met. This is essential to maintaining offshore wind energy's long-term competitiveness and to realising its full potential in addressing climate change by superseding the use of non-sustainable fossil fuels.

1.1.4. Wind Turbine Support Structures

A wind turbine's support structure comprises the wind turbine tower and the substructure, in this case a monopile. The monopile is the most commonly used support structure for offshore wind turbines [19]. Despite depth limitations, monopiles are used in deeper waters with larger turbines [20]. Their popularity is driven by low engineering, fabrication, and installation costs [21]. The technical and economic depth limit of monopiles is uncertain, with studies suggesting thresholds that vary by site conditions, turbine size, and technology [20, 22, 23]. As technical advancements continue to push this boundary, ensuring economic feasibility requires greater material efficiency, while maintaining safety and long-term reliability is essential.

A monopile-type substructure consists of primary and secondary structures. Primary structures ensure integrity: the large-diameter pile in the seabed, the connection interface (transition piece or flange), and the tower. Figure 1.3 illustrates all main components of a monopile support structure and two common configurations. These primarily differ in how the monopile connects to the tower, either via a grouted transition piece or a direct flanged connection. Secondary structures aid functionality and access, such as boat landings, J-tubes, platforms, and ladders. They do not affect the global load path.

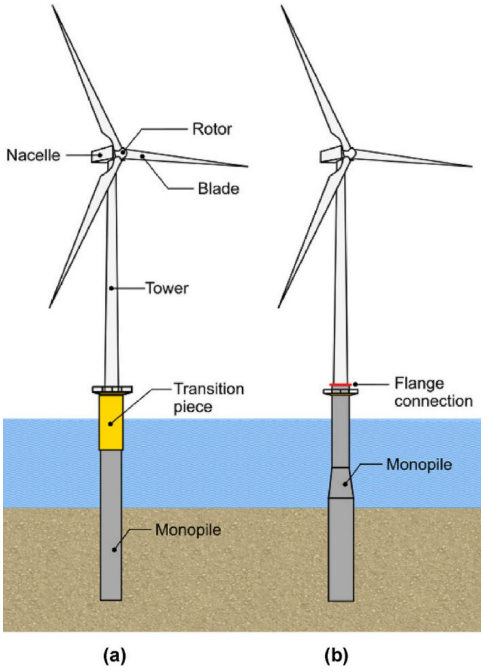

Figure 1.3: Schematic representation of two turbines with two different types of monopile support structures [24].

1.2. Problem Statement

The increase in Support Structure (SuS) size, as described in previous sections, induces significant changes in the dynamic responses of their SuSs, particularly monopiles, altering how they interact with environmental forces such as wind and waves. These changes have implications not just for structural performance but also for the reliability of current engineering models, assumptions and design codes.

An emerging concern is the growing importance of low-frequency, high-wave-height excitation. While it has little effect on smaller turbines, it becomes critical for larger ones because the natural frequency of the SuS decreases with increasing size.

Please Note: In this thesis the term natural frequency refers specifically to the first bending-mode natural frequency of the SuS, comprising both the turbine tower and the substructure and Rotor Nacelle Assembly (RNA), unless explicitly specified otherwise.

This shift in dynamic behaviour challenges existing modelling assumptions and design standards, particularly those relating to turbine availability non-operational periods, when aerodynamic damping is

low. Treating availability in a simplified or deterministic manner may lead to excessive conservatism for smaller SuSs, inflating costs, but more critically, to non-conservatism for larger SuSs. In such cases, designs may underestimate the contribution of rare, fatigue-critical storm conditions to overall fatigue damage, falling short of International Electrotechnical Commission (IEC) safety requirements, reducing fatigue life, and jeopardising structural integrity

1.3. Research Objectives and Questions

This thesis focuses on wave-induced fatigue loading of monopile-based offshore wind turbines, with an emphasis on evaluating how turbine-to-turbine availability variances influence design fatigue life. To capture this effect, Supervisory Control And Data Acquisition (SCADA) data is used to derive turbine-specific availability profiles. The primary objective is therefore twofold:

- To assess, using SCADA-derived availability profiles, whether current modelling assumptions regarding turbine non-operational variance are adequate for smaller monopile-based turbines.
- To evaluate their validity for modern, large-sized turbines and identify potential non-conservatism in fatigue life predictions.

Therefore, the main research question is:

How does turbine-to-turbine availability variance, derived from SCADA data, influence fatigue life estimates for monopile-based offshore wind turbines of different sizes, compared to current deterministic design methods?

The sub-questions that were identified to answer the main research question are the following:

1. **Literature and Theory:** How do current design methods and standards represent fatigue damage during non-operational periods and related uncertainty in wave-induced response-loads?
2. **Variance in Availability:** How can turbine-to-turbine variance in non-operational periods be identified, classified, and modelled from SCADA availability data, and how is this variance best represented in a fatigue assessment?
3. **Combined Analysis of Loads and Turbine Availability:** When turbine-specific availability profiles, as quantified in sub-question 2, are combined with frequency-domain simulations, how do the resulting fatigue life estimates for 8 MW and 14 MW monopile turbines compare with those derived from the deterministic design methods?
4. **Implications for Design Methods:** Do the findings suggest revisions to how fatigue damage is quantified in the non-operational Design Load Case (DLC), particularly with respect to turbine availability assumptions and the calibration of Partial Safety Factors (PSFs) for future generations of offshore wind turbines?

1.4. Thesis Outline

In order to answer the main research question and sub-questions, this thesis is divided into five chapters. An outline of the chapters that will follow is given below:

- **Chapter 2: Current Design Process and Treatment of Uncertainty**
  Provides an overview of the structural design process and criteria. How uncertainties are introduced by modelling environmental loading and fatigue damage. It evaluates the current method of representing non-operational periods. The use of PSF to account for these uncertainties is also addressed.
- **Chapter 3: Methodology**
  Details the research approach, simulation tools, and models, with particular focus on the use of SCADA-derived turbine-specific availability profiles. It explains how an adapted availability model was coupled with frequency-domain fatigue simulations to quantify the impact of availability variance on fatigue design life.
- **Chapter 4: Results**
  Presents the outcomes of the SCADA-driven availability analysis, including observed turbine-to-

turbine variance in non-operational periods, the influence of availability model hyperparameters on simulated fatigue damage variance, and fatigue life predictions for 8 MW and 14 MW turbines over the full design life.

- **Chapter 5: Discussion**
  Discusses the implications of the results for current design standards, availability assumptions, and the calibration of PSFs, including whether these should be revised to reflect availability-driven fatigue variance. The chapter then places the findings in the broader context of offshore wind turbine design by comparing availability variance-driven fatigue damage variance with other key sources of uncertainty. The chapter includes analyses to test the validity of key assumptions, providing additional context for interpreting the findings and also acknowledges the limitations of the thesis.
- **Chapter 6: Conclusions and Recommendations**
  Summarises the key findings of the thesis, discusses their relevance to existing design practices and standards, and revisits the research questions to reflect on how they have been addressed. Finally, it provides recommendations for future research.

2

Current Design Process and Treatment of Uncertainty

This chapter explains the design constraints of offshore wind turbine support structures and gives an overview of the current design process and which uncertainties the current design process includes and how they are modelled. Subsequently, the current approach to applying PSFs within the design framework is reviewed. Additionally, wave loads and the associated sources of uncertainty are discussed.

2.1. Design Constraints

One of the most important design parameters in the structural design of SuS is the first natural frequency, f_1. This is the frequency at which a structure naturally tends to oscillate when disturbed and is primarily governed by the structure's mass and stiffness properties. In practice, the first bending mode dominates the global dynamic response and directly influences fatigue loading. Ideally, the natural frequency should be far from operational and environmental excitation frequencies to avoid resonance. Resonance occurs when dynamic loads oscillate at or near the structure's natural frequency, causing amplified structural vibrations and increased fatigue damage. However, placing the natural frequency as far away as possible from the excitation frequencies is challenging to achieve in practice due to structural and economic constraints.

The first natural frequency of a monopile-based turbine can be approximated using an analytical formula for a cantilever column with a lumped top mass, shown in Equation (2.1) [25].

$$f_1 \approx \frac{1}{2\pi}\sqrt{\frac{3.04EI}{(0.227\bar{\lambda}_m L_{\text{tot}} + M_{\text{top}})L_{\text{tot}}^3}} \tag{2.1}$$

Where:

- E is the Young's modulus of steel used in the support structure.
- I is the second moment of area of the cross-section of the tower and/or monopile.
- $\bar{\lambda}_m$ is the mass per unit length of the SuS.
- $L_{\text{tot}} = L_{\text{monopile}} + L_{\text{tower}}$ is the total length of the system.
- M_{top} is the top mass that represents the RNA.

Although this equation does not give exact results, it gives intuitive insight into how the natural frequency of a turbine tends to shift as it grows in size. It shows that as L_{tot} increases and/or M_{top} becomes heavier (due to bigger, heavier, rotor and generators for larger turbines), the natural frequency decreases.

Scaling-Effects in Operational-Excitation Forces for Large Offshore Wind Turbines

Modern turbines are developing towards larger rotor diameters, taller towers, and are being installed in deeper waters. These changes result in increased structural flexibility and a reduction in the first natural frequency f_1. At the same time, excitation frequencies due to turbine operation also decrease.

The main operational excitation frequencies are:

- **1P** – Rotor rotational frequency (typically 0.1-0.3 Hz).
- **3P** – Frequency of blade passing the the tower (typically 0.3-0.6 Hz).

Excitation Bandwidth of Environmental Loads

Offshore wind turbines are also subjected to dynamic loading from the environment. Both the wind and wave loading contribute to cyclic loads and are typically characterised using spectral models:

- **Kaimal spectrum** - Describes turbulent wind energy, described in [26].
- **Joint North Sea Wave Project Spectrum (JONSWAP)** - Describes wave energy distribution, described in [27].

These environmental spectra contribute energy across a frequency band, making it important to avoid not just resonance with the 1P and 3P frequency bands but also regions of high environmental spectral energy overlap with f_1.

This interaction is visualized in Figure 2.1, which shows the 1P and 3P excitation frequency bands, overlaid with the Kaimal (orange) and JONSWAP (black) spectra. The figure also includes an arrow indicating natural frequencies shift downward for larger turbines in deeper waters.

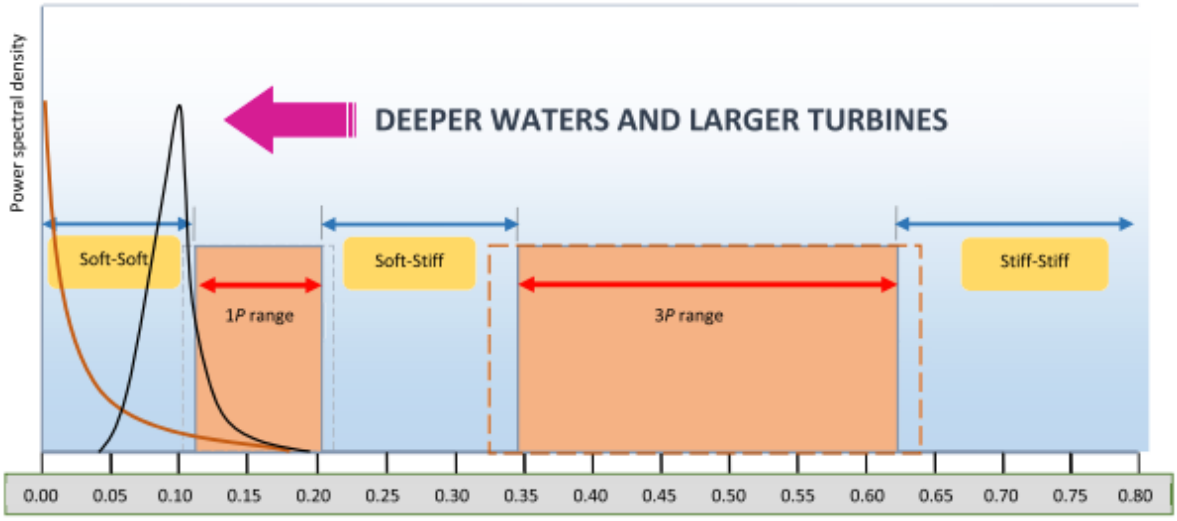

Figure 2.1: Schematic overview of excitation frequencies (environmental, 1P and 3P), design regions (soft–soft, soft–stiff, stiff–stiff), and trend of decreasing natural frequency for larger turbines in deeper waters [28].

From this, three typical design regions are defined:

- **Soft–soft**: $f_1 <$ 1P - Generally avoided due to strong wave-induced fatigue.
- **Soft–stiff**: 1P < f_1 < 3P - Targeted as design region for modern large turbines.
- **Stiff–stiff**: $f_1 >$ 3P - Requires excessive stiffness and material use and therefore economically unfeasible for large turbines.

As structural flexibility increases and excitation frequencies decrease with increasing turbine size, avoiding resonance becomes more challenging. This imposes increasingly tight constraints on the design of the SuSs.

Influence of Aerodynamic Damping

When a turbine is in operation, there will be significant aerodynamic damping in the fore-aft direction due to the rotor, while there is relatively low damping in the side-to-side direction. Consequently, excitation of the system in the fore-aft direction will be damped. However, due to faults, low or high winds, or maintenance, a turbine may become non-operational and lose this aerodynamic damping, making it susceptible to wave excitation because of the absence of aerodynamic damping.

Resonant Sea States and Fatigue Critical Conditions

As turbines grow in size, the monopile substructure becomes increasingly flexible, leading to lower first natural frequencies f_1 and longer corresponding natural periods T_n. When T_n shifts toward longer peak wave periods, there is the possibility of resonance with increasingly higher waves. This can become problematic during non-operational states, where damping is limited.

These higher H_s sea states cannot exist at lower T_p due to the wave steepness limit (i.e. waves will break before becoming unrealistically steep). This is illustrated in Figure 2.2, it shows the scatter distribution of significant wave height H_s versus peak period T_p. The colour scale indicates the number of occurrences per sea state, based on long-term European Centre for Medium-Range Weather Forecasts Reanalysis (ERA)-5 hindcast simulations at a representative offshore site. The most frequently occurring sea states cluster around $T_p = 3\text{-}5.5$ s, where wave heights are constrained to less than approximately 2 m due to the wave steepness limit.

As f_1 decreases and T_n increases with larger turbines, the risk of resonance shifts toward these less frequent, long peak wave-period sea states. Although rare, these sea states are capable of having higher H_s and could cause significant resonant amplification of structural response, especially during non-operational conditions, when there is low aerodynamic damping. Their rarity does not diminish their impact. As shown in [29], such conditions could dominate fatigue damage consumption for large monopile-based turbines.

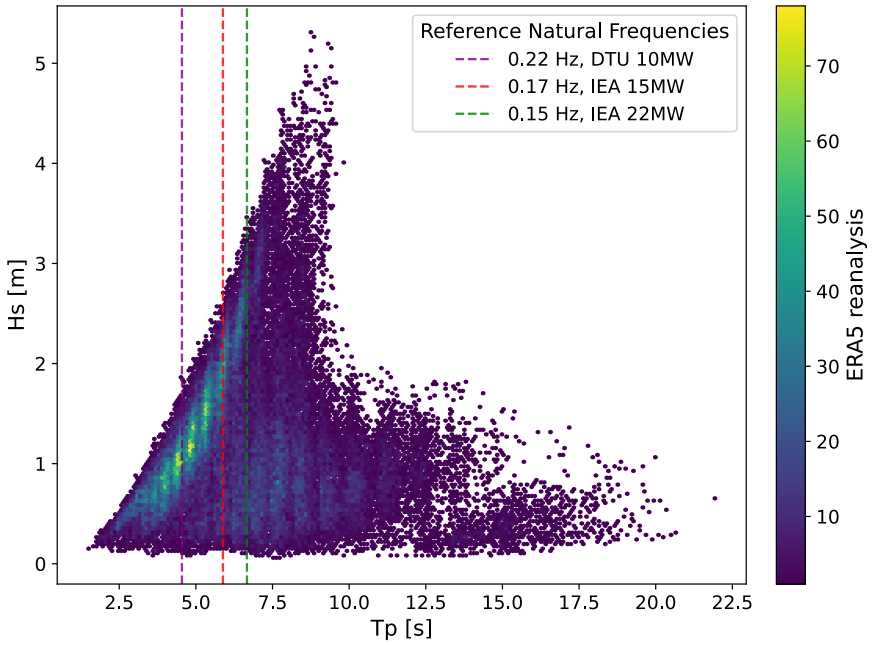

Figure 2.2: Scatter-plot of significant wave height H_s and peak period T_p, with colour-indication of number of observations in the hindcast data. With three example natural frequencies of large monopile-based reference turbines.

2.2. Current Design Process for Offshore Wind Turbine Support Structures

The design process of a turbine's SuSs is governed by a framework of engineering standards and industry guidelines to ensure safety, reliability, and regulatory compliance. These standards establish the principles for structural design, load modelling, safety margins, and certification requirements. So that a consistent and efficient approach across different projects, companies and geographical regions is achieved.

Central to this framework are the standards issued by the IEC, which provide the foundational methodologies and design requirements for wind turbine design. For offshore wind turbines, these are ex-

panded with specific requirements that address the specific needs of offshore environments. Additionally, classification authorities such as DNV offer detailed design and verification guidance. These organisations not only influence design practices but also serve as certifying bodies. The most relevant standards for this thesis are:

- **IEC 61400-1** – *Design Requirements for Wind Turbines*: Covers general design principles for on- and offshore turbines, forming the basis for structural analysis and load case definitions.
- **IEC 61400-3-1** – *Design Requirements for Fixed Offshore Wind Turbines*: Supplements IEC 61400-1 with offshore-specific loading and design considerations.
- **DNV-ST-0126** – *Support Structures for Wind Turbines*: Used for fixed-bottom offshore support structure design.
- **DNV-ST-0437** – *Loads and Site Conditions for Wind Turbines*: Defines standard methods for environmental load modelling.
- **DNV-RP-C205** – *Environmental Conditions and Environmental Loads*: Provides guidance on environmental load calculations for offshore structures.
- **DNV-RP-C203** – *Fatigue Design of Offshore Steel Structures*: Defines methodologies for fatigue assessment of offshore structural components.
- **Eurocode 1993-1-9** – *Design of steel structures: Fatigue*: Also defines methodologies for fatigue assessment of steel structural components.

Designs have to comply with these standards in order to obtain certification, to be allowed to be built and also to ensure safety and reliability.

From this framework of design standards, a sequence of steps that define the design process for the SuS are found. The main steps and how to deal with uncertainty are identified and schematically represented in Figure 2.3.

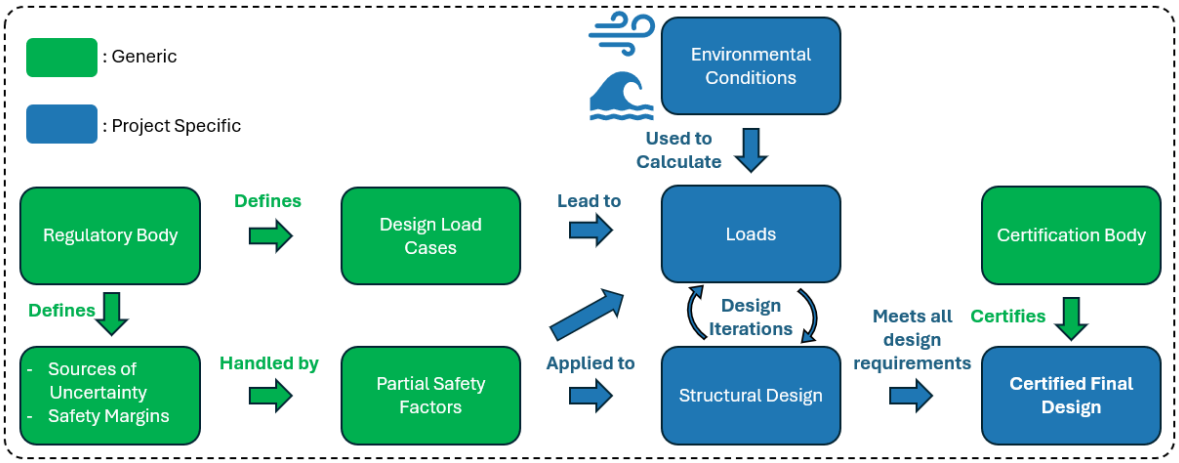

Figure 2.3: Flow diagram of the SuS design process and the current approach of handling uncertainty.

Examples of regulatory bodies are: IEC and International Organization for Standardization (ISO). These bodies define the sources of uncertainty and how to account for them. The current method uses PSFs, these account for uncertainty in material properties, environmental conditions, and modelling assumptions. Using this method provides a standardised and deterministic approach to handle uncertainty.

However, this approach also has its limitations, since the use of fixed PSFs can hide the actual influence of uncertainty on structural performance, especially when not all sources of uncertainty are properly identified. By embedding all uncertainty into (calibrated) factors applied post hoc, the interaction between probabilistic input distributions and response loads is not explicitly evaluated. Also, the influence of site-specific sources of uncertainty, such as the rarity of fatigue-critical near-resonance sea states is not accounted for.

The steps of the design process shown above will be discussed in the following sections. First, the limit states that define DLCs and motivate the use of PSFs are introduced in Section 2.2.1, followed by DLCs in Section 2.2.2. After that, the PSFs methodology will be discussed in more detail in Section 2.3.1.

2.2.1. Limit States

The design requirements of SuSs are specified by different types of limit states that define structural performance requirements under specified conditions for different failure mechanisms. The two most critical limit states are the Ultimate Limit State (ULS) and the Fatigue Limit State (FLS), which will be evaluated later in more depth. Limit states are typically described using the limit state function, shown in Equation (2.2).

$$G(X) = R(X) - S(X) \tag{2.2}$$

Where $G(X)$ is the limit state function, $R(X)$ represents the structural resistance (i.e., the capacity of the structure to withstand loads), and $S(X)$ represents the load. Both R and S are functions of a set of input parameters X, which may include material properties, geometric dimensions, environmental conditions, and modelling uncertainties. These parameters may be treated as fixed values or modelled as random variables to capture inherent variance and (model) uncertainty. As long as $G(X) > 0$, the structure is considered to be in a safe state. However, if $G(X) \leq 0$, the limit state is exceeded, indicating that the structure has either failed or reached an unacceptable probability of failure (P_f), and is therefore deemed unsafe.

In reliability-based design, this failure probability is often expressed via the reliability index β, which relates to P_f through the standard normal cumulative distribution function: $P_f = \Phi(-\beta)$. For turbines, the IEC 61400-1 standard sets a target reliability index of $\beta_t = 3.3$, corresponding to an annual probability of failure of: $P_f = 5 \cdot 10^{-4}$. This reliability index target is motivated by the nature of offshore wind turbines as unmanned infrastructure with limited environmental or societal consequences in the event of failure. Offshore oil and gas platforms are manned, economically valuable, and environmentally risky. Therefore, they target stricter reliability indices: $\beta_t = 3.7$ ($P_f = 10^{-4}$) up to $\beta_t = 4.7$ ($P_f = 10^{-6}$) depending on the cost of safety measures.

To achieve the desired reliability indices, PSFs are used. To account for uncertainty in $R(X)$, the material PSF, γ_m, is used. For uncertainty in $S(X)$, the load PSF, γ_f, is used. These factors are calibrated based on probabilistic analyses and can also differ per limit state considered. Therefore, the calibration of safety factors in offshore wind reflects a balance between acceptable risk and economic feasibility.

This concept is illustrated in Figure 2.4, where the part of the probability distribution of $G(X) \leq 0$ determines P_f.

The calibration of safety factors and how uncertainty is handled in design will be evaluated more in depth in Section 2.3.1.

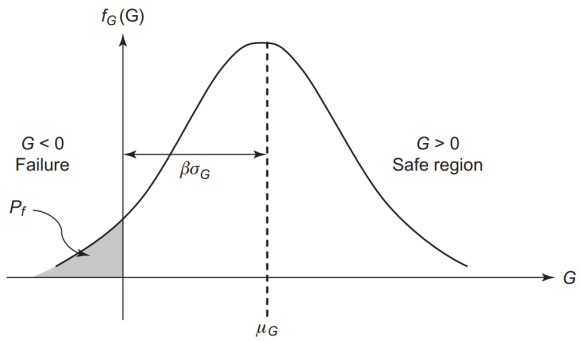

Figure 2.4: Graphical representation of a limit state with one design parameter, indicating P_f and reliability index β [28].

Ultimate Limit State

The ULS evaluates the maximum load bearing capacity of a structure under extreme loading conditions. Failure in ULS implies immediate collapse or plastic deformation that makes the structure unfit for use or unsafe. ULS conditions include extreme wind events and extreme wave impacts.

Fatigue Limit State

The focus of this thesis is the FLS, the FLS addresses the degradation of structural performance due to repeated loading over time. Unlike ULS, fatigue failure occurs gradually through the accumulation of damage caused by cyclic stress ranges, i.e. cyclic (time-varying) applied loads. This limit state is particularly critical for offshore wind turbines, which experience millions of load cycles over their operational life. Modern offshore wind turbines are often considered FLS-critical [30].

The fatigue limit state is typically assessed using the Palmgren-Miner linear damage accumulation hypothesis, described in [31]. Palmgren-Miner's rule assumes that fatigue damage accumulates linearly with the number of stress cycles and that failure occurs when the cumulative damage reaches a critical threshold, commonly taken as unity. The Palmgren-Miner's rule is expressed as:

$$D = \sum_{i=1}^{n} \frac{n_i}{N_i} \tag{2.3}$$

Where n_i is the number of cycles applied at a specific stress range $\Delta\sigma_i$, and N_i is the number of cycles to failure at that same stress range as given by the SN-curve, which, together with its uncertainty will be evaluated in Section 2.3.1. The structure is deemed to have failed in the FLS when D reaches or exceeds 1.0. The stress ranges $\Delta\sigma$ are obtained via cycle-counting algorithms in the time-domain, such as the rainflow-counting algorithm, described in [32]. For the frequency-domain, the empirical Dirlik's method is often used, described in [33]. This method uses power spectral density to estimate fatigue damage by statistically modelling the distribution of stress range cycles.

Other Limit States

The other two limit states for turbines are:

- **Serviceability Limit State (SLS):** Ensures conditions are safe for personnel to enter the turbine (e.g., limiting wind speeds and wave heights).
- **Accidental Limit State (ALS):** Considers the structural response under accidental events (e.g., boat-impacts or fire).

2.2.2. Design Load Cases

To ensure the SuS is able to withstand the different limit states introduced in the previous section, each limit state is evaluated using DLCs. Each DLC represents a specific combination of turbine operational state (e.g., normal/operational, faulted, or parked/non-operational) and site-specific environmental conditions. These operational states, defined by characteristic wind speed thresholds, govern the dynamic behaviour of the turbine.

Within each DLC, relevant environmental variations, such as wind speed V, significant wave height H_s, peak wave period T_p, and wind and wave directions, are represented using discretisation or lumping approaches. Wind conditions are typically discretised into bins, where continuous ranges are divided into intervals. In contrast, wave conditions (H_s, T_p) are often reduced using lumping techniques, such as damage-equivalent optimisation, to define representative sea states, as described in [34]. For each combination of wind and wave conditions, representative simulations are performed to evaluate structural response. This approach ensures that the full environmental distribution is sufficiently covered while limiting the number of computationally expensive simulations required.

For the verification of the FLS, the topic of this thesis, DLCs defined by the IEC, such as 1.2 (normal operation), 6.4 (parked/standstill/idling), and 7.2 (parked/standstill with fault conditions), are particularly important, because those collectively account for the majority of load cycles experienced by the SuS over the design life. These DLCs and how they are collectively combined to get the total fatigue damage will be explained in more detail in the next subsection.

Current Approach of Calculating Fatigue Damage

The current approach of calculating fatigue damage, using the DLC definitions provided by IEC, depends on several design-parameters determined in the design phase of a turbine and project, which are listed below:

- **Cut-in wind speed** $V_{\text{cut-in}}$: Minimum wind speed at which the turbine begins generating power (typically 3–4 m/s).
- **Cut-out wind speed** $V_{\text{cut-out}}$: Maximum wind speed above which the turbine shuts down for safety reasons (typically 25–32 m/s).
- **Availability ratio** α: Fraction of time the turbine is operational and able to produce power within the operational wind speed window. Due to faults and maintenance, a wind turbine is not always available for power production in the operational wind speed window. Typical availability values are around 95%, this value is determined on a per project basis.

So, the two ranges of wind speeds outside the operational wind speed window: $V \notin [V_{\text{cut-in}}, V_{\text{cut-out}}]$, that is, the low-wind parked regime and the high-wind shutdown regime are entirely determined by wind speed thresholds defined by the turbine's design. In contrast, situations when the turbine is parked within the operational wind speed window arise from factors such as faults, scheduled maintenance, or grid curtailment, and thus cannot be inferred from wind conditions alone. Instead, this represents a stochastic process within the operational range, governed by the turbine's availability and may vary across turbines within the same wind farm.

The current approach to simulating fatigue damage is schematically illustrated in Figure 2.5. The blue section at the bottom represents the proportion of the turbine's design life during which it is operational, i.e., producing power, scaled by the availability ratio α. The white section on the right corresponds to the duration when the turbine is unavailable, or non-operational, due to maintenance, faults, or grid curtailment or similar events.

Fatigue damage from the operational and non-operational state is then computed based on the (lumped) hindcast simulations and linearly scaled according to the associated duration in the N-year design life. These contributions are aggregated to estimate the total design life fatigue damage.

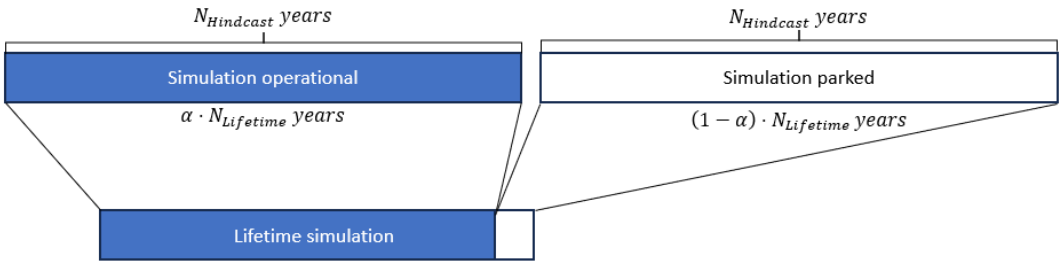

Figure 2.5: Schematic overview of the current methodology for estimating fatigue damage under both operational and non-operational conditions using environmental hindcast data.

The upper part of the figure shows how environmental conditions are modelled using a set of hindcast years, typically ranging from 25 to 40 years. This same hindcast dataset is used to simulate both operational and non-operational conditions. Implicit in this approach is the assumption that the hindcast data are statistically representative of all operational states, including non-operational, even though the non-operational proportion may constitute only a small fraction of the total design life. For example, with an availability of 95%, the non-operational exposure amounts to just 1.25 years in a 25-year design life. Compared against a 40-year hindcast dataset, the non-operational period represents only approximately 3.1% of the total hindcast data. This limited coverage raises the question of whether the damage experienced in a relatively short non-operational period can be approximated by scaling the non-operational damage obtained by simulating the long-term historical distribution.

This is illustrated in Figure 2.6, which compares the SCADA availability data for two turbines within the same wind farm over a period of 4.5 years. As shown, the turbines experienced different sea states

during non-operational periods, particularly in the less frequent but high H_s near-resonance conditions. These conditions are of particular concern, as they can contribute disproportionately to the consumption of fatigue life, as discussed in Section 2.1.

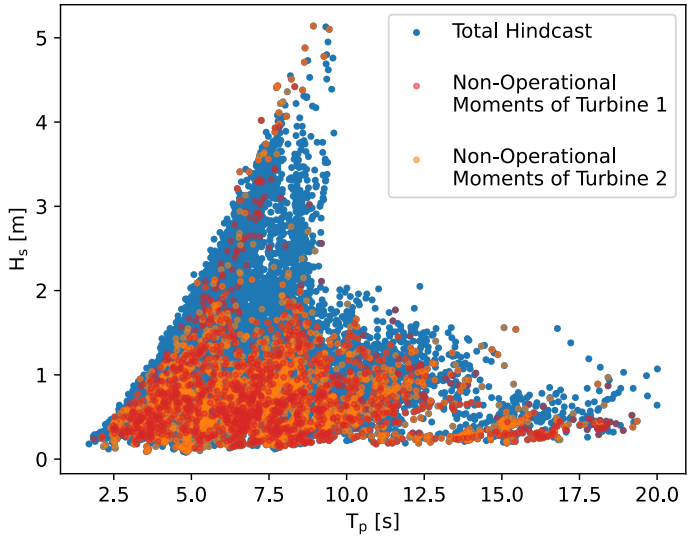

Figure 2.6: Different observed non-operational moments for two wind turbines within the same wind farm when compared to ERA-v5 hindcast of the same period.

DNV recommends assuming the availability of the 90% or 100% turbines, whichever results in greater fatigue damage, as a conservative basis for the design, unless actual availability data is available [35]. In [35], the authors demonstrated that this assumption tends to produce pessimistic fatigue life estimates, since real-world turbine availability is typically higher than 90%. In this study, offshore wind turbine availability was modelled as a random variable following a beta distribution with a mean of 93%, and its influence on fatigue damage was evaluated using the DTU 10 MW reference turbine with a first natural frequency of 0.22 Hz.

Many large modern turbines exhibit even lower natural frequencies than the DTU 10 MW reference wind turbine, which, as explained in Section 2.1, makes these larger turbines even more susceptible to infrequent high H_s (near-)resonance sea states, resulting in high fatigue damage events during non-operational periods. These (near-)resonant load cases could contribute disproportionately to total fatigue damage but are smoothed out in conventional fatigue assessment methodologies. Thereby, it could underestimate turbine-specific exposure to these rare fatigue damage-intensive sea states and underestimate turbine-specific fatigue damage.

2.3. Characterisation and Treatment of Uncertainty in Offshore Wind Turbine Design

The design of the SuS of a turbine is affected by multiple sources of uncertainty that influence its reliability. For example, these uncertainties could arise from: variances in environmental conditions, simplifications in modelling approaches, and natural scatter in material properties and fatigue behaviour.

A distinction is made between two types of uncertainty:

- **Aleatoric uncertainty**, also known as inherent or irreducible uncertainty, arises from the stochastic nature of physical processes such as wind turbulence, wave heights, and random sea states. These uncertainties are intrinsic to the environment and cannot be reduced through improved modelling or data collection.

- **Epistemic uncertainty**, or reducible uncertainty, is knowledge based and can, in principle, be reduced with better measurements, models, or improved understanding. Examples include limited site-specific soil data, simplified load and structural models, and assumptions made in the estimation of fatigue damage.

The correct identification and treatment of these uncertainties in the design of a SuS is key to ensure that the safety and reliability requirements, specified by IEC, are met. This section focuses on:

- Section 2.3.1: Which uncertainties are handled in current design practices and how these are incorporated in the design process through PSFs.
- Section 2.3.2: How recent research seeks to improve their calibration, especially for wave-sensitive large monopile-based wind turbines.

2.3.1. Partial Safety Factors Approach in IEC-61400

Section 2.2.1 discussed how reliability-based design handles uncertainties via the limit state function and the defined P_f. The PSF approach used in the IEC-61400 design standards is based on the safety factors background document by Sørensen and Toft, [36], which outlines a probabilistic framework incorporating various sources of uncertainty using a probabilistic model, this document focuses on smaller-sized onshore turbines. The following subsection details how specific types of uncertainty are represented in the current PSF calibration. An overview is given in Table 2.1.

Table 2.1: Uncertainties handled in current standards, D standing for deterministic, N for normally distributed, LN for lognormally distributed [36].

Variable	Distribution	Expected Value	STD / COV	Comment
Δ	N	1	$COV_{\Delta} = 0.30$	Model uncertainty in Palmgren-Miner's rule
m_1	D	3	–	Slope of SN-curve (region 1)
$\log K_1$	N	from $\Delta\sigma_D$	$\sigma_{\log K_1} = 0.2$	Intercept of SN-curve (region 1)
m_2	D	5	–	Slope of SN-curve (region 2)
$\log K_2$	N	from $\Delta\sigma_D$	$\sigma_{\log K_2} = 0.2$	Intercept of SN-curve (region 2)
$\Delta\sigma_C$	D	Depends on material and detail considered	–	Fatigue strength
X_{wind}	LN	1	COV_{wind}	Model uncertainty in wind load
X_{SCF}	LN	1	COV_{SCF}	Model uncertainty in stress concentration factor

The uncertainties described in Table 2.1 will be evaluated in the next subsections.

Model Uncertainty in Palmgren-Miner's Rule

Fatigue life estimation is affected by uncertainties associated with the models used to represent fatigue damage mechanisms. These are typically referred to as resistance model uncertainties. One key source of such uncertainty is related to the application of Palmgren-Miner's rule, which was introduced in Section 2.2.1. Palmgren-Miner's rule assumes linear damage accumulation and thus does not account for load sequence effects or interaction between cycles. Furthermore, the rainflow counting algorithm used to determine the stress ranges also introduces uncertainty. These modelling limitations are captured by introducing a model uncertainty, denoted as Δ, which is assumed to follow a normal distribution with an expected value of 1.0 and a coefficient of variation of 0.30, as shown in Table 2.1.

Material Properties Uncertainty

The material properties used in the FLS evaluation are influenced both by the base material and the type of welded detail considered. Fatigue resistance is typically characterised by SN-curves, which describe the relationship between stress range (S or $\Delta\sigma$) and the number of cycles to failure (N). The main properties of materials for FLS evaluation are called the Wöhler-slope m and the intercept K. The Wöhler-slope is the slope of the SN-curve when plotted in log log scale. The intercept K is defined at a reference amount of cycles N_{ref}, for Eurocode-1-9 N_{ref} is defined at $2 \cdot 10^6$. These properties naturally vary due to aleatoric material property scatter, as well as epistemic uncertainties related to manufacturing processes and quality control.

Figure 2.7 illustrates different SN-curve representations commonly used in fatigue design for a specific welded steel detail. The bilinear formulation (blue/red) reflects the approach used in Eurocode 3-1-9 and other design standards, where a change in slope occurs at the knee point N_D. In contrast, the

pivoted linear curve (green) represents a common industry practice, where the SN-curve is simplified by linearising through the knee point using a single slope ($m = 5$). This simplification avoids discontinuities and facilitates easier integration into fatigue damage accumulation models, particularly in combination with frequency domain models. The assumption for this simplification is that it is assumed that most stress cycles for wind turbines are in the high-cycle stress range and therefore the low-cycle stress range is of less importance, this is also justified by the fact that this assumption is also conservative. If a linearised SN-curve were drawn using a Wöhler slope smaller than that of the high-cycle part of the bilinear curve ($m < 5$), the simplified curve would lie above the original curve in the high-cycle regime. This would imply higher allowable stresses for the same number of cycles and therefore underestimate fatigue damage. Such a representation would not be conservative, since most stress cycles occur in the high-cycle range. For this reason, the simplified linearisation through the knee point is only considered acceptable when using $m = 5$, which ensures conservatism relative to the bilinear formulation.

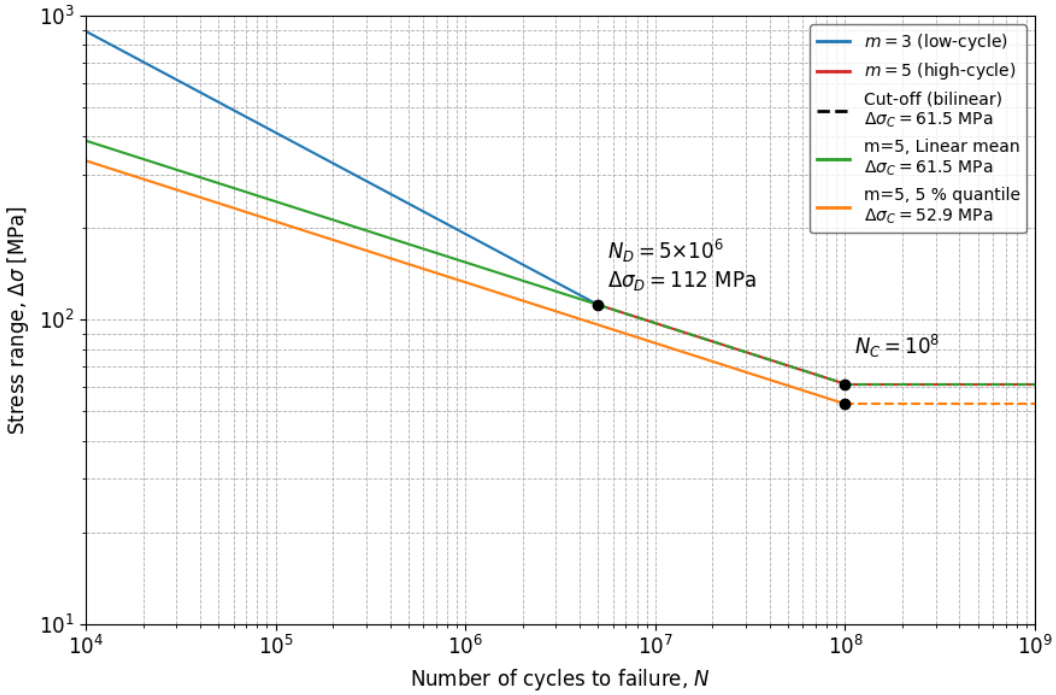

Figure 2.7: SN-curves for welded joints showing bilinear (blue/red), linear (green), and 5% quantile (orange) representations. The bilinear curve transitions at $N_D = 5 \times 10^6$ with a cut-off at $N_C = 10^8$ and $\Delta\sigma_C = 61.5$ MPa. The linear and quantile curves (both with $m = 5$) illustrate common industry practice and statistical lower bounds.

The orange curve shows a 5% quantile representation that reflects the probabilistic treatment of material scatter in the intercept K, which is typically modelled using a lognormal distributions. These distributions avoid non-physical negative stress values and capture the skew of empirical fatigue test-data. Uncertainties in the SN-curve parameters, particularly in the intercept, have a direct influence on predicted fatigue life and are therefore treated stochastically, whereas the slope of the SN-curve is treated deterministically.

In the PSF background document to IEC-61400-1, the authors incorporate this uncertainty into the calibration of partial safety factors. When using the mean SN-curve, a material factor of $\gamma_m = 1.25$ is applied. Alternatively, if a conservative SN-curve shifted two standard deviations below the mean is used (to represent a 5% quantile), the corresponding factor is reduced to $\gamma_m = 1.04$.

Load Modelling

The two primary sources of fatigue loading for monopile-based turbines are wave-induced and wind-induced forces. As wave loads are the main focus of this thesis, this subsection summarises the wave load modelling approach relevant to this thesis and will introduce how load model uncertainties are accounted for.

Wave kinematics and the free-surface profile are first modelled using Airy linear wave theory, described in [37]. Linear wave theory provides water particle velocities and accelerations beneath the free surface based on wave height, period and water depth. These kinematics are used as input to the Morison equation. The Morison equation is an empirical relationship to describe the hydrodynamic forces per unit length f acting on slender structures, such as monopiles, exposed to both wave and current loading, further described in [38]. It accounts for two main components of force: the inertia force and the drag force, which is shown in Equation (2.4).

$$f = C_m \rho \frac{\pi}{4} d^2 \dot{u} + C_D \frac{1}{2} \rho d u |u| \tag{2.4}$$

Where ρ and d are the density of water and diameter of the structure respectively. The inertia term represents the force caused by the acceleration of the water particles $\dot{u}$. This includes the Froude-Krylov force, which is caused by the pressure field created by the undisturbed wave motion, and the additional mass force caused by the acceleration of water around the structure due to its presence, which is captured by the dimensionless inertia coefficient C_m, which is defined as $C_m = 1 + C_a$, where C_a is the added mass coefficient.

The drag term represents the force caused by the flow of water past the structure. It depends on how fast the water is flowing relative to the structure and increases with the square of the water speed. This force also depends on the drag coefficient C_D, which reflects the shape and roughness of the structure.

The Morison equation assumes that the structure is slender, such that the structure does not significantly disturb the incident wave field, i.e. diffraction and radiation effects are neglected. In [14], DNV defines the slenderness limit for the applicability of Morison's equation as $\frac{\pi d}{\lambda} < 0.5$, where λ is the wavelength. When this threshold is exceeded, as is increasingly the case for large-diameter monopiles, diffraction effects become significant and must be accounted for. In such cases, diffraction theory, such as the MacCamy–Fuchs approach, described in [39], is typically applied to capture the hydrodynamic loading more accurately.

To account for the variation of force with depth, the force per unit length obtained from the Morison equation should be calculated at multiple depths. These values can then be numerically integrated over the entire depth to determine the total hydrodynamic force acting on the structure.

Load Model Uncertainties

In numerical simulations, load model uncertainties are caused by the imperfect representation of environmental conditions and structural dynamics. Factors influencing the wave-loading uncertainty include limitations in hindcast data, inaccuracies in wave spectral models used to reconstruct sea states, and simplifications in wave kinematics and hydrodynamic loading, such as those introduced by Airy wave theory and the Morison equation.

These uncertainties are typically represented using multiplicative stochastic variables applied to the load effect, often assumed to follow lognormal distributions with a mean of 1.0 and a specified Coefficient Of Variation (COV). This probabilistic treatment allows their influence to be incorporated into reliability-based design frameworks by adjusting the partial safety factors to maintain the desired target reliability level.

For the FLS, which is the main focus of this thesis, the uncertainty in fatigue loads, or stress ranges is incorporated by the γ_f PSF. γ_f is based on the amount of variation in the loads which Sørensen and Toft defined in [36] for a fatigue critical detail such as a weld or flange as shown in Equation (2.5).

In Equation (2.5), two sources of uncertainty are considered: the recently introduced wind load model uncertainty and Stress Concentration Factor (SCF) uncertainty. The latter arises from the estimation of local stress concentrations at welded details or geometric discontinuities, which are often fatigue critical. These concentrations are typically accounted for using an SCF, which may be influenced by modelling assumptions, simplifications, limited fidelity, or weld imperfections. To capture this, a model uncertainty factor X_{SCF} is introduced. This factor is assumed to follow a lognormal distribution with a mean of 1.0, and a coefficient of variation, denoted as COV_{SCF}, which depends on the specific detail considered.

$$COV_{\text{load}} = \sqrt{COV_{\text{wind}}^2 + COV_{\text{SCF}}^2} \tag{2.5}$$

In [36], it is stated that the COV_{load} typically falls within the 15-20% interval and with $\gamma_m = 1.25$, they recommended γ_f to be equal to 1.00.

The PSFs calibrated through this procedure in [36] were based on a relatively small onshore wind turbine. These turbines are only subjected to wind-induced loading. As such, the original calibration does not incorporate offshore (site-)specific wave response-loading variance in non-operational conditions, as explained in Section 2.2.2.

2.3.2. PSF Calibration for Offshore Wind Turbines

Calibrating PSFs for offshore wind turbines requires accounting for the relevant uncertainties. In [40], the author incorporated wave-load model uncertainty into the calibration of PSFs for offshore wind turbines. Instead of applying the partial safety factors γ_f and γ_m as defined in the IEC standards and the associated PSF background document, the author adopted the Fatigue Design Factor (FDF) approach described by DNV. The relationship between the FDF and the PSFs of IEC is given in Equation (2.6).

$$FDF = (\gamma_f \gamma_m)^m \tag{2.6}$$

In Equation (2.7), the fatigue limit state design equation, the FDF is coupled with the design parameter **z**, the pile thickness, such that the design condition is satisfied when the equation equals zero.

$$G(z) = 1 - \sum_{i=U_{in}}^{U_f} \sum_{j=\Delta\sigma_1}^{\Delta\sigma_{cut}} \frac{n_{i,j,k} p_i FDF T_L}{K_{c1} \Delta\sigma_{i,j,k}^{-m_1}} - \sum_{i=U_{in}}^{U_f} \sum_{j=\Delta\sigma_{cut}}^{\Delta\sigma_\infty} \frac{n_{i,j,k} p_i FDF T_L}{K_{c2} \Delta\sigma_{i,j,k}^{-m_2}} = 0 \tag{2.7}$$

The pile thickness that satisfies the deterministic design condition in Equation (2.7) reflects the application of the FDF and thereby incorporates the prescribed safety factors. This chosen pile thickness is then used as input to the probabilistic limit-state formulation in Equation (2.8). In other words, the FDF (and thus the partial safety factors) is carried into the probabilistic limit state equation through adjusting the pile thickness. By modelling the wave-load model uncertainty, X_{wave}, explicitly as a random variable with $COV_{\text{wave}} = 0.10$ in Equation (2.8), the reliability calibration accounts for this uncertainty while capturing the heightened sensitivity of large offshore wind turbines to hydrodynamic excitation.

$$\begin{aligned} g(\mathbf{z}, t) = \Delta &- \sum_{i=U_{\text{in}}}^{U_{\text{out}}} \sum_{j=\text{TI}_{0.05}}^{\text{TI}_{0.95}} \sum_{k=\Delta\sigma_1}^{\Delta\sigma_{\text{cut}}} \frac{n_{i,j,k} p_{i,j} t}{K_1 \left(\Delta\sigma_{i,j,k}\right)^{-m_1}} \left(X_{\text{SCF}} X_{\text{dyn}} X_{\text{wave}}\right)^{m_1} \\ &- \sum_{i=U_{\text{in}}}^{U_{\text{out}}} \sum_{j=\text{TI}_{0.05}}^{\text{TI}_{0.95}} \sum_{k=\Delta\sigma_{\text{cut}}}^{\Delta\sigma_\infty} \frac{n_{i,j,k} p_{i,j} t}{K_2 \left(\Delta\sigma_{i,j,k}\right)^{-m_2}} \left(X_{\text{SCF}} X_{\text{dyn}} X_{\text{wave}}\right)^{m_2} \end{aligned} \tag{2.8}$$

In Equation (2.8), the summation is carried out over all fatigue sea states i with turbulence intensity j, each occurring with probability $p_{i,j}$, and for all stress cycle bins k. In [40], availability was reduced from 100% to 95% to represent 5% non-operational periods using the standard IEC DLC treatment. This reduction caused the contribution of wave-induced fatigue damage to increase from 21.6% to 51.6%, showing that even a modest fraction of downtime can make non-operational periods dominant in fatigue accumulation. For the DTU 10 MW reference turbine considered in the same study, a FDF of 3 was found to be just sufficient to reach the target failure probability of $P_f = 10^{-3}$. This result suggests that for more wave-sensitive turbines in wave-dominated sites, the current IEC fatigue PSF ($\gamma_f = 1.0$) may no longer provide adequate reliability.

However, because the method used in [40] assigns a fixed probability to non-operational sea states, it may under-represent turbine-specific exposure to rare, fatigue-critical conditions. A more realistic approach is to use stochastic downtime periods, replacing the current non-operational DLC, so that

rare fatigue-critical sea states are explicitly represented. The methodology developed in this thesis, introduced in Chapter 3, extends this idea by using SCADA-driven availability profiles to represent non-operational periods explicitly in the fatigue design process.

The limitation of the current design method, which uses an average mean fatigue damage over long-term hindcasts is further amplified when considering long-term shifts in wave climate due to climate change. Traditional design assumes stationary wave conditions, with distributions unchanged over time. But evolving wind patterns may alter wave heights and storm frequencies during a turbine's life [41]. This effect is particularly important for larger turbines, for which fatigue-critical sea states coincide more with rare storm conditions. In [41], the authors propose addressing climate-change-induced uncertainty in wave loads by applying geographically dependent PSFs.

3

Methodology

The previous chapter covered design constraints, the design process, treatment of uncertainty, and the limitations of DLCs in representing fatigue-critical non-operational sea states. Building on this, the present chapter sets out the methodology developed to quantify the impact of such events and addresses the main research question:

How does turbine-to-turbine availability variance, derived from SCADA data, influence fatigue life estimates for monopile-based offshore wind turbines of different sizes, compared to current deterministic design methods?

The chapter is organised as follows, Section 3.1 describes the data sources and simulation software used. Section 3.2 presents the existing availability model and its theoretical basis. Section 3.2.1 introduces the adaptation of the availability model and methodology to quantify the effect of availability variance in fatigue damage for two sizes of monopile-based offshore wind turbines. Finally, the underlying assumptions are summarised in Section 3.4.

3.1. Data, Models and Simulation Tools Descriptions

This section will introduce the different types of data, models and simulation tools used in this thesis.

3.1.1. Metocean Data

To simulate the various DLCs, metocean data is used. The dataset employed in this study is derived from the ERA-5 reanalysis and covers a 25-year period, ranging from January 2000 to January 2025, at one offshore site located in the Dutch North Sea. The data has a 3-hourly resolution and includes the following parameters:

- V_{Lat}: Latitudinal wind speed measured at 10 m above sea level, in m/s.
- V_{Long}: Longitudinal wind speed measured at 10 m above sea level, in m/s.
- T_p: Peak wave period, representing the most energetic wave component of the JONSWAP spectrum, in seconds.
- H_s: Significant wave height, defined as the average height of the highest one-third of waves, in meters.
- MWD: Mean wave direction, measured in degrees clockwise from the north.

Instead of using the latitudinal and longitudinal wind speed components directly, they are transformed into wind speed magnitude and direction. To estimate the wind speed at the different hub heights for the different turbine sizes considered in this study, the power law, as described in Section 1.1.3, is applied using an exponent of α_p=0.12, as recommended by DNV. The peak enhancement factor γ of the JONSWAP is calculated using the methodology described in [14].

The data is accessed through Oceanum, a platform that provides oceanographic and meteorological datasets via an Application Programming Interface (API). However, due to missing values of H_s and T_p in the swell wave components, these were excluded from the scope of this thesis.

A description of the metocean climate of the site considered in this thesis, including scatter plots, wind and wave roses, and wind speed distributions, is provided in Appendix B.

3.1.2. SCADA system

The SCADA system for turbine operational data is Polaris, it collects turbine operational data in 10 minute statistics such as mean, minimum, maximum and standard deviation. Variables that were used in this thesis are the measured wind speed at the turbine hub and the turbine's operational state. Around 4.5 years of SCADA data is used of a representative wind farm of about 70 offshore wind turbines. The wind farm is located at the same site from which the metocean data was retrieved.

3.1.3. Offshore Wind Turbine Models

In this study, wave-induced fatigue damage is investigated for two monopile-based turbines, with rated power outputs of 8 and 14 MW. These turbines represent current and future-scale offshore wind turbine sizes. The main parameters of both turbine models are summarised in Table 3.1.

Table 3.1: Key parameters for both offshore wind turbine models.

Turbine size [MW]	**8**	**14**
Rotor diameter [m]	167	236
Hub height [m]	115	146
Cut-in wind speed [m/s]	3	4
Cut-out wind speed [m/s]	28	32

3.1.4. Simulation Software

To model the loads on the turbine models described earlier, an in-house frequency-domain model developed by Siemens Gamesa is used. In this model, the RNA is represented as a concentrated mass. The soil stiffness is linearised using fixity depth or py-soil springs, depending on the specific turbine model. The drag term in the Morison equation is linearised by the Borgman method, described in [42]. The frequency domain model converts wave-spectral data into structural response using Dirlik's Method, described in [33].

The frequency domain model, which is based on [43], achieves computational speeds that allow complete load assessments to be carried out in minutes. This is fast compared to the multiple hours typically required by time-domain solvers. In the frequency domain model, wind effects are incorporated via user-defined aerodynamic damping, which depends on wind speed and direction (fore–aft and side-to-side). The wind loads are represented using precomputed wind Damage Equivalent Loads (DELs). These are obtained by the use of an aerodynamic simulation tool, run under wind-only conditions. For each environmental input combination, the quadratic superposition method, which is shown in Equation (3.1) and described by [44], is applied to combine wind and wave loads into a single DEL for each sector.

$$DEL_{tot} \approx \sqrt{{DEL_{wave}}^2 + {DEL_{wind}}^2} \tag{3.1}$$

This setup enables full hindcast simulations. The main focus of this thesis is the variance of wave-induced response loads and its influence on current design practices and fatigue design life assumptions, particularly during non-operational periods. During such periods, wind loads are assumed to be insignificant compared to wave loads and therefore not considered. For both turbine models, a single Wöhler slope of m=5 is applied.

3.2. Existing Availability Model for Component Reliability

As already explained in Sections 2.1 and 2.2.2, operational availability differences between turbines, could lead to fatigue damage variance across turbines within the same wind farm. While the DLCs in the current method already consider non-operational states, they do not fully capture a real-world variance in unavailability, and could fail to reflect the disproportionate impact of near-resonant, high H_s

sea states that are particularly intensive in fatigue damage. The resulting variance in fatigue damage originates from two key sources:

- Different turbines in the same wind farm are non-operational for different amounts of time when compared to each other.
- Different turbines in the same wind farm are non-operational at different moments in time when compared to each other, with the possibility of one being non-operational in low H_s non-resonant sea states, while the other could be non-operational in high H_s (near-)resonant sea states and thus accumulate fatigue damage at a higher rate.

To address this, load estimation approaches that include availability-variance could be incorporated into the design framework. Various models have been developed with the aim of predicting component failures and power availability. One could extend these models to also incorporate load calculations. One of such models is the model described in [45]. This paper describes a Markov-based reliability framework designed to estimate wind turbine system availability by accounting for subsystem failures and repair processes. It uses a Markov chain where the main turbine components, such as the gearbox, generator, blades, are modelled with three states: available, degraded, and unavailable. Other components without condition-monitoring systems, like electronics, are modelled with two states: available and unavailable.

Each of these components is modelled as a stochastic process. The time to failure is exponentially distributed with a failure rate $\lambda_{1,n}$ with n indicating the component number, the Mean Time To Failure (MTTF) for a two-state system is defined in Equation (3.2). $\lambda_{2,n}$ is used to describe the probability of transition from degraded state to unavailable state. The repair process is also modelled with a rate μ_n, the Mean Time To Repair (MTTR) is defined in Equation (3.3)

$$\text{MTTF}_n = \frac{1}{\lambda_{1,n}} \tag{3.2}$$

$$\text{MTTR}_n = \frac{1}{\mu_n} \tag{3.3}$$

A schematic overview of these two and three-state systems is given in Figure 3.1 below.

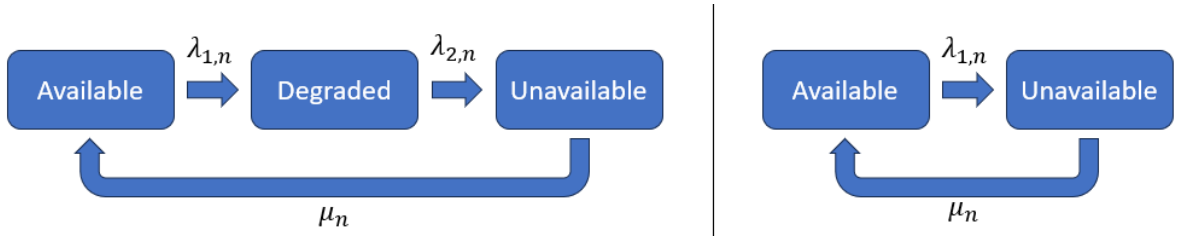

Figure 3.1: Schematic overview of three and two-state systems.

By assuming that the failure of any single component will result in the entire system being non-operational, the components are modelled as being connected in series. Under this assumption, the component-level models can be combined into a Markov model to represent the overall turbine or system. The system-level failure and repair rates $\lambda_{1,eq}$ and μ_{eq} (and corresponding MTTF_{eq} and MTTR_{eq}) can be derived from individual component rates with Equations (3.4) and (3.5) shown below.

$$\lambda_{1,eq} = \sum_i \lambda_{1,i} \tag{3.4}$$

$$\mu_{eq} = \sum_i \mu_i \tag{3.5}$$

If one assumes a two-state failure process for all components, the turbine is either operational (state 0) or non-operational (state 1). When the steady-state probabilities of the Markov model are denoted by the state vector $\bar{\pi} = [\pi_0, \pi_1]$, Equation (3.6) holds.

$$\mu_{eq}\pi_0 = \lambda_{1,eq}\pi_1 \tag{3.6}$$

Then the total probability of being in either the operational or non-operational state must always sum to one:

$$\pi_0 + \pi_1 = 1 \tag{3.7}$$

By rearranging and substituting Equations (3.2) to (3.6) into Equation (3.7), one obtains Equation (3.8).

$$\pi_1 = \frac{1}{1 + \frac{\lambda_{1,eq}}{\mu_{eq}}} = \frac{1/\lambda_{1,eq}}{1/\lambda_{1,eq} + 1/\mu_{eq}} \tag{3.8}$$

Which can also be expressed like:

$$\text{Availability} = \pi_1 = \frac{\text{MTTF}_{eq}}{\text{MTTF}_{eq} + \text{MTTR}_{eq}} \tag{3.9}$$

With models like the one described above, one can randomly assign non-operational periods that are different per turbine or iteration considered, based on real component failure or downtime data. By combining this model with DELs per sea state one can quantify the influence of variance in availability on fatigue damage.

3.2.1. Adaptation of the Availability Model for Fatigue Damage Assessment

To quantify the variance in fatigue damage due to availability and wave response-loading variance, this thesis uses a SCADA data-driven approach comparing two turbine sizes, so that the effect of upscaling turbine size on the validity of current design methodologies can be investigated. The methodology adapts the availability model introduced by [45], originally designed to simulate turbine availability based on component-level failure and repair processes, where key turbine subsystems are represented as two- or three-state Markov chains.

In this thesis, however, the model presented in [45] is altered. Due to the unavailability of failure rate data, but the availability of SCADA data including operational states and downtime durations in 10 minute intervals, a data-driven approach is adopted. Rather than deriving stochastic non-operational periods from component failures, non-operational periods are directly inferred from SCADA data. As a result, only the two-state failure model is used. This adaptation to a SCADA-driven approach is further supported by the fact that not all non-operational periods result from component failures; they may also result from grid curtailments or environmental access restrictions (e.g., wave height limits). This adaptation results in the availability model becoming a discrete time Markov chain rather than a continuous time Markov chain. In [35], the authors used Markov Chain Monte Carlo in the form of Gibbs sampling, which also allowed for varying the metocean data.

By first quantifying turbine-to-turbine variance in non-operational periods from SCADA availability data, the approach directly addresses Research Question 2: *"How can turbine-to-turbine variance in non-operational periods be identified, classified, and modelled from SCADA availability data, and how is this variance best represented in a fatigue assessment?"*

Second, by using the above-described availability model in combination with frequency-domain fatigue simulations, one can answer Research Question 3: *"When the availability profiles obtained in sub-question 2 are combined with frequency-domain fatigue simulations, how do the resulting fatigue design-life estimates for 8 MW and 14 MW monopile turbines compare with those derived from current deterministic design methods?"*

A schematic overview of the model and its four main components is given in Figure 3.2. The four main components and their steps will be introduced in the following subsections.

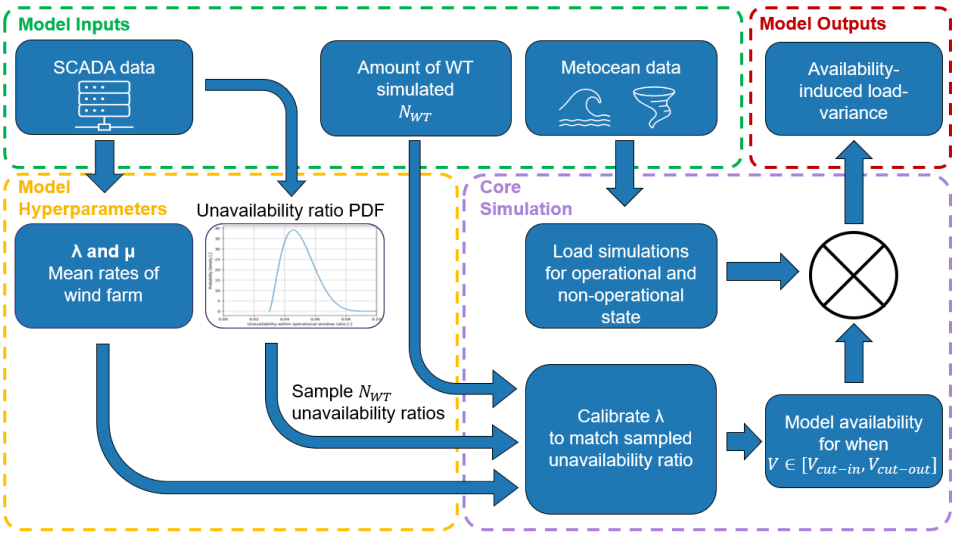

Figure 3.2: Schematic overview of the implementation of the availability model.

Model Inputs

The model uses three primary inputs: 10 minute SCADA data, 3 hourly metocean data and the number of turbines, N_{WT}, simulated. For a workable analysis, the original SCADA operational availability data, containing more than 10 distinct operational states, was simplified into three main states:

- **State 1:** Wind speed is inside the operational wind speed window and the turbine is operational: $V \in [V_{cut-in}, V_{cut-out}]$, thus the turbine has significant aerodynamic damping in the fore-aft direction due to the rotor, it still has low aerodynamic damping in the side-to-side direction.
- **State 2:** Wind speed is inside the operational wind speed window and the turbine is non-operational: $V \in [V_{cut-in}, V_{cut-out}]$, thus the turbine has little aerodynamic damping in the fore-aft direction. These non-operational periods are not determined by environmental conditions such as wind speed and thus could be assumed to be random across turbines.
- **State 3:** Wind speed is outside operational wind speed window and the turbine is non-operational: $V \notin [V_{cut-in}, V_{cut-out}]$, thus the turbine has little aerodynamic damping in the fore-aft direction. These non-operational periods are determined by environmental conditions and can therefore not be assumed to be random across turbines.

To illustrate this, these distinct operational states are illustrated in Figure 3.3, together with a generic wind speed Probability Density Function (PDF).

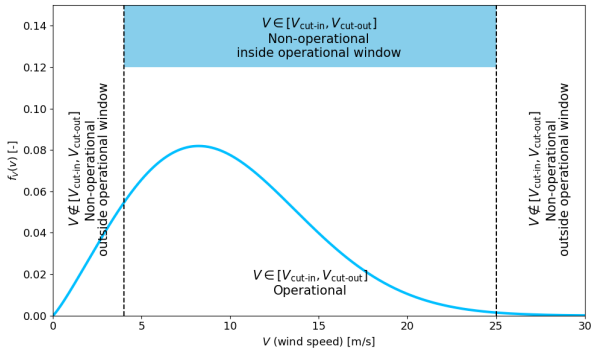

Figure 3.3: Typical two-parameter Weibull wind speed probability density function f_v showing operational subpopulations defined by cut-in and cut-out wind speeds (adapted from [35]).

Due to the 10 minute averaging interval of the SCADA data, the precise timing of operational state changes within an interval with a state-change cannot be determined. Therefore, all intervals in which a turbine was recorded to change operational state were excluded from further analysis. This filtering resulted in the exclusion of approximately 4.2% of all 10 minute intervals. These omitted periods occurred predominantly around the cut-in wind speed threshold. This way a state transition is defined as a difference between states from one 10 minute window to the next 10 minute window.

Turbines which were recorded to have an unavailability ratio greater than 10% were excluded in order to focus on turbines whose behaviour remains within the nominal design envelope. The influence of this assumption and its implications are examined in greater detail in Chapter 5.

To integrate the SCADA and metocean datasets, the mismatch in temporal resolution first had to be addressed. The SCADA data are available at a 10-minute resolution, whereas the metocean dataset has a coarser resolution of 3 hours.

Many of the non-operational periods identified in the SCADA data are therefore shorter than one metocean time step. To resolve this, the metocean values were forward filled, meaning that each 3-hour measurement was repeated. Since one 3-hour interval corresponds to 18 SCADA samples of 10 minutes each, every metocean data point was replicated 18 times to align with the SCADA time series. Implicit in this procedure is the assumption that metocean conditions remain stationary within each 3-hour time window.

Model Hyperparameters

Simulating stochastic turbine unavailability directly, rather than modelling component-level failures, introduces several model hyperparameters. These parameters influence how turbine operational patterns are reproduced in the simulation, and their effects must therefore be examined carefully. To do this, the turbines in the SCADA dataset were randomly divided into two equally sized subsets (50/50 split). One subset was used to estimate the probabilities of transitioning to the non-operational state, λ_i, and transitioning back to the operational state, μ_i. The other subset was reserved for testing the model's performance. These hyperparameters are evaluated in greater detail in the following paragraphs.

Unavailability Ratio PDF: Following the approach as proposed by [35], turbine unavailability is modelled using a beta distribution. Since unavailability is a proportion bounded between 0 and 1, the beta distribution is well-suited due to its flexibility and finite support. As noted in [35], typical offshore wind turbine unavailability is expected to be between 4% and 10%. Based on this, a generic beta distribution for the unavailability ratio is defined between 0.04 and 0.10, a mean of 0.055 (i.e., 94.5% availability) and a standard deviation of 0.01. The influence of the choice of the unavailability distribution is later shown in Section 5.2. For each simulation realisation, a value U_{target} is sampled from this distribution. This predetermined target unavailability serves as criteria against which the simulated unavailability U_{sim} will later be compared during calibration. The beta distribution is shown in Figure 3.4.

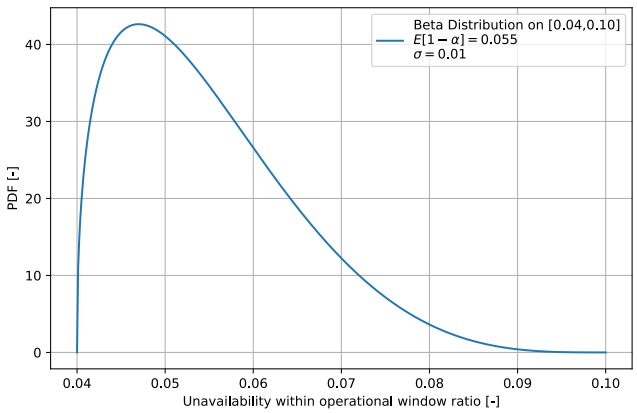

Figure 3.4: Beta distribution used for representing unavailability ratio within the operational window.

Classification of Non-Operational Periods: Another hyperparameter is the classification of non-operational periods. In the original model of [45] each turbine component has its own transition rate $\lambda_{1,n}$ and recovery rate μ_n. In [46], the authors analysed turbine fault statistics and classified turbine-level downtimes into two classes per component: minor events (shorter than 24 h) and major events (longer than 24 h). The number of non-operational duration classes, and the placement of these class boundaries could affect the results. Therefore, these hyperparameters should be carefully evaluated against observed availability- and fatigue damage variances. These hyperparameters can be adjusted in order to match the fatigue damage obtained when matching SCADA data availability profiles with frequency domain simulations.

The three modelling choices regarding the classification of non-operational periods that must be made are:

- Grouping strategy for non-operational classes, i.e. how non-operational durations are grouped into classes based on their duration by using either linear or logarithmic spacing.
- Number of non-operational classes $N_{\text{i}} \in \{1, \ldots, 5\}$.
- Position of the class boundaries (only relevant when $N_{\text{i}} > 1$).

The four statistics derived from the SCADA data availability patterns are referred to as the target variables, the calibration procedure aims to reproduce these variables as closely as possible. These variables are listed below:

- μ_{Dam}: Mean fatigue damage.
- COV_{Dam}: Coefficient of variation of fatigue damage.
- μ_{NP} : Mean duration of non-operational periods.
- $\sigma_{T_{\text{NP}}}$: Standard deviation of non-operational durations.

The unavailability error is defined as the difference between the simulated unavailability U_{sim} and the sampled target unavailability U_{target}, which is shown in Equation (3.10).

$$\text{Unavailability error} = U_{\text{sim}} - U_{\text{target}}. \tag{3.10}$$

Transition and Recovery Rates: Once a strategy is determined to classify non-operational periods, the rates for each non-operational class i follow directly from the SCADA data:

$$\lambda_i = \frac{S_i}{T_{\text{op}}} \tag{3.11}$$

$$\mu_i = \frac{\Delta t}{\bar{d}_i} \tag{3.12}$$

Where S_i is the number of transitions into class i, T_{op} is the total operational time in minutes, $\Delta t = 10$ minutes is the SCADA sampling interval, and $\bar{d}_i$ is the mean duration of events in class i.

The transition rates are a Poisson process, which is a continuous time process. While the SCADA data is in discrete time, for each discrete time step Δt the probability p of at least one state transition is given by Equation (3.13).

$$p = 1 - e^{-r_i \Delta t} \tag{3.13}$$

In which r_i is the corresponding transition rate. It is assumed that the influence of multiple transitions taking place within the same time step is negligible.

Calibration Procedure: Both linear and logarithmic grouping strategies are evaluated for $N_{\text{i}} = 1$–5, each configuration being simulated six times with different random seeds and 100 turbine iterations per run. The calibration progresses through three successive steps. First, the full set of strategy/bin-count combinations is explored. Next, a multi-criteria trade-off is applied: the preferred configuration is the one that reproduces the target variables as close as possible, while keeping the error in simulated unavailability $U_{\text{sim}} - U_{\text{target}}$ acceptably low. Finally, for that configuration (and only when $N_{\text{i}} > 1$), the bin

boundaries are tuned to refine the match in the fatigue damage COV while keeping the unavailability error as small as possible. The resulting calibrated model is benchmarked against all target statistics' observed values. The results of this calibration process is evaluated in Section 4.2.

Core Simulation

The core simulation starts with four inputs:

- The fleet-wide class-specific transition rates λ_i and μ_i that were derived from SCADA data.
- The number of turbines, (N_{WT}), being simulated, too few will result in unstable statistics, while too much will result in unnecessary high computational costs.
- A random sample of length N_{WT} from the unavailability ratio PDF.
- The metocean data used to do the load calculations.

First, the full metocean hindcast dataset is used to generate aDELs for each time step with an unique environmental condition. This is done for two cases: a turbine that is 100% available throughout the operational wind speed window and a turbine that is 0% available within the same window. The DELs generated by this are later used in combination with the availability model.

Because state 3 is determined by the wind speed, namely whenever $V \notin [V_{cut\text{-}in}, V_{cut\text{-}out}]$, it is assumed that its occurrence is identical for every turbine that shares the same metocean data. By making this assumption one assumes no wake effects. Consequently, the stochastic availability model, whose purpose is to describe stochastic downtimes, is not applied to these time instances. Instead, all time steps classified as state 3 are removed before the availability simulation is run, so that the model is only applied when the wind speed is inside the operational wind-speed window.

At the beginning of each iteration (ranging from 1 to N_{WT}), a scalar correction factor C is determined. This C is determined such that scaling all transition rates to non-operational state λ_i, while keeping the transition-to-operational-state rates μ_i unchanged, yields a long-term probability of being non-operational equal to the sampled unavailability ratio. U_{target}. The U_{target} is drawn from the unavailability ratio PDF. Using these scaled transition rates, turbine-specific availability time traces are generated.

The long-term unavailability of a turbine is given analytically by Equation (3.14).

$$U(C) = 1 - \prod_i \frac{\mu_i}{\mu_i + C\lambda_i} \tag{3.14}$$

Because $U(C)$ is strictly increasing and continuous in C, given that $C \geq 0$, Equation (3.15) has an unique solution, which can be found using a root-finding algorithm such as Brent's method, which is described in [47].

$$U(C) = U_{\text{target}} \tag{3.15}$$

Once the scaling factor C is determined, the failure rates are updated as $\lambda_i^{\text{scaled}} = C\lambda_i$. These rescaled rates define a Markov chain that generates a stochastic availability trace over the design life of a turbine. This trace acts as a binary switch: at each time step, it selects either the operational or non-operational DEL, producing an unique fatigue load history for each turbine.

After the simulation has produced its series of operational and non-operational states within the operational wind speed window (states 1 and 2), the previously excluded state 3 intervals, where the wind speed is outside the operational wind speed window, are reinserted at their original time stamps.

Model Outputs

For each realisation, the core simulation returns a time history of DELs spanning the entire time period of the metocean dataset. These DELs are converted to fatigue damage by applying Palmgren Miner's rule. Repeating the procedure N_{WT} times, each run drawing an independent unavailability ratio and its associated correction factor C, produces a unique combination of DELs, thereby enabling quantification

of the fatigue-damage variance arising from availability variance across a wind farm. A larger N_{WT} narrows the confidence intervals of the ensemble statistics, albeit at a higher computational cost.

The resulting damage estimates are then compared against the current design practice, where fatigue damage is calculated using the DNV 90/10 assumption (i.e., 90% operational and 10% non-operational).

3.3. Full Design Life Fatigue Damage Simulations

The availability model obtained by following the described calibration procedure in the last section is used to evaluate the fatigue damage over the full design life, which is assumed to be 25 years, of a 8 and 14 MW turbine size under identical environmental conditions. This enables an evaluation of how upscaling of turbine size affects deterministic fatigue design life predictions compared to predictions with random non-operational periods.

3.4. Summary of Assumptions

Several assumptions have been made throughout the methodology to quantify the wave-induced fatigue damage variance caused by variances in availability. This section summarises the most important assumptions:

- The design life of all turbines is assumed to be 25 years.
- The wind speed is assumed to be constant over the simulated turbines, this means that the non-operational state due to the wind speed being outside of the operational wind speed window is the same for all turbines. This implies for example no wake effects.
- By forward filling the 3-hourly metocean data to match the SCADA data resolution of 10 minutes it is assumed that the metocean data is stationary within 3 hours.
- It is assumed that the metocean data is not varying between turbines at the same moment in time.
- It is assumed that the influence of multiple events taking place at the same time is negligible.
- Turbine availability is assumed to be in-between 4% and 10% and the unavailability ratio can be described by a beta distribution bounded between 4% and 10%. This neglects turbines with severe faults and so only as-expected turbine availability is taken into account.
- It is assumed that non-operational periods within the operational wind speed window of a turbine are a purely random process, and not correlated to previous events or metocean data.
- It is assumed that the unavailability profiles retrieved from SCADA data are representative for a full design life.
- During non-operational periods, wind loads are assumed to be negligible compared to wave loads and are therefore not considered.
- When a turbine's operational ratio changes (either reduced or increased), it is assumed that the relative distribution between short and long non-operational periods remains constant. Only the transition rates λ_i to all non-operational classes are scaled accordingly.

4

Results

This chapter presents the results from the availability-induced fatigue damage variance. The observed availability variance and the resulting fatigue damage variance are evaluated first. The calibration of the availability model's hyperparameters and their influence on the model's output are then examined. The calibrated availability model is subsequently applied to predict the fatigue damage and its variance for two different turbine sizes over a full design life.

4.1. Observed Availability- and Resulting Fatigue Damage Variance

Figure 4.1 shows the operational history of three turbines within the same wind farm over a period of nine months. In the figure, blue indicates that a turbine was operational and producing power. Red indicates that the turbine could have produced power, as the wind speed was within the operational wind speed window, but it did not. Green indicates that the wind speed was outside the operational wind speed window, and the turbine was non-operational.

The figure shows different non-operational periods of varying durations within the operational window for each turbine. While most non-operational periods outside the operational wind speed window are shared across the turbines, some differences still exist. This observation differs from the assumption that these periods could be treated as constant across turbines within the same wind farm. A more detailed evaluation of this assumption and its validity is provided in Chapter 5.

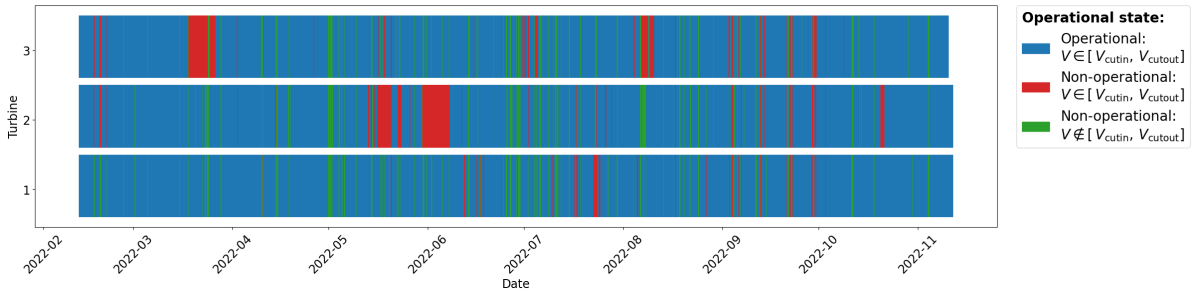

Figure 4.1: Observed availability profiles over nine months of three turbines within the same wind farm.

The observed availability profiles from SCADA data are combined with pre-computed DELs from frequency-domain simulations (decribed in Section 3.1.4). The metocean conditions from the hindcast at the same time and location as the recorded SCADA data are used to obtain sector-wise fatigue damage estimates. In practice, this means that for every non-operational period identified in the SCADA data, the corresponding metocean conditions, together with the turbine being unavailable, are used to generate the DEL associated with that moment. By aggregating these results, the variance in fatigue damage across the 8 MW wind farm is obtained per directional sector along the turbine circumference, as illustrated in Figure 4.2. Due to confidentiality, the values are normalised so each sector's mean is equal to 1.0. It was found that the $[-15°, 15°)$ sector was the driving sector on average, meaning that it accumulated the most fatigue damage during this period.

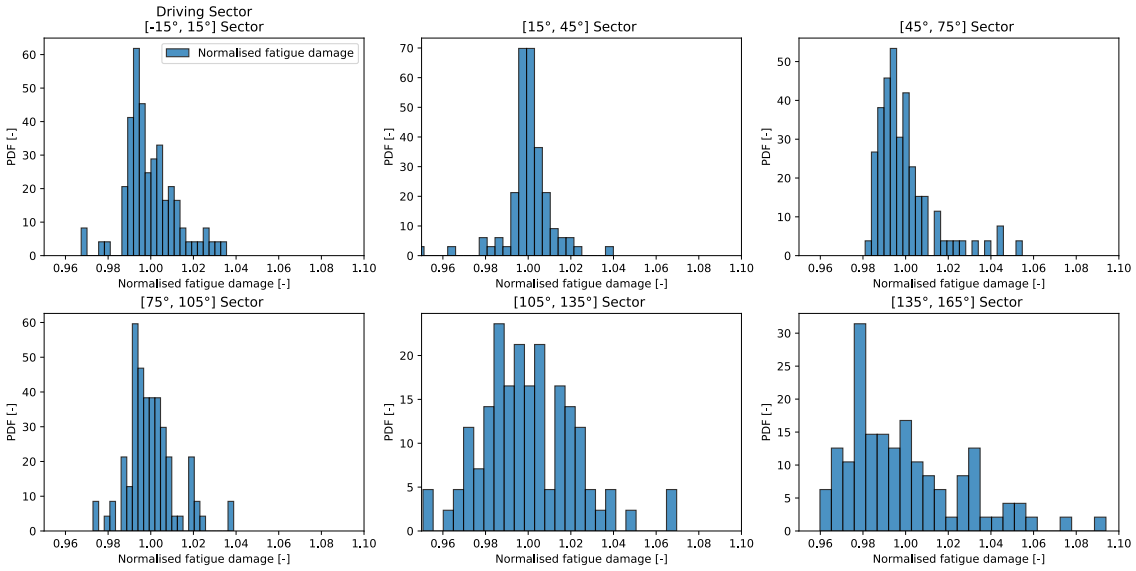

Figure 4.2: Normalised fatigue damage per sector at mudline when SCADA data availability profiles are matched with frequency domain simulations

By doing this, the target variables for the availability model calibration procedure can be quantified. The observed values of these target variables are listed in Table 4.1. Please note that, due to normalisation, all mean fatigue damage values, μ_{Dam}, are defined as 1.0.

Table 4.1: Target variables obtained by matching SCADA data availability patterns with frequency domain simulations.

Target Variable	COV_{Dam} $[-15°, 15°)$	COV_{Dam} $[15°, 45°)$	COV_{Dam} $[45°, 75°)$	COV_{Dam} $[75°, 105°)$	COV_{Dam} $[105°, 135°)$	COV_{Dam} $[135°, 165°)$	μ_{NP} [h]	σ_{NP} [h]
Observed value	0.012	0.011	0.016	0.013	0.018	0.022	Confidential	Confidential

4.2. Calibration of Availability Model Hyperparameters

The results of the calibration procedure described in Section 3.2.1 will be presented in this section. First, the influence of the number of non-operational classes on the target variables μ_{Dam} and COV_{Dam} will be evaluated. Subsequently, the influence on the unavailability error will be examined. At the end, the influence of the number of non-operational classes on mean non-operational duration, μ_{NP}, and the standard deviation of non-operational durations, σ_{NP}, will be evaluated.

Afterwards, the number of non-operational classes will be chosen based on the performance against the target variables and it concludes with a comparison on all target variables of the calibrated model and observed values.

4.2.1. Influence of Number of Non-Operational Classes on Mean and COV of Fatigue Damage

Figure 4.3 shows the influence of non-operational duration binning strategies (linear and logarithmic) and the number of non-operational classes (1 to 5) on the simulated mean fatigue damage (left column) and the COV of fatigue damage (right column) for the sector with the highest mean fatigue damage. The results of all sectors can be found in Appendix C. The mean values are normalised with respect to the observed values, or target values, obtained by using the availability profiles of the SCADA data as input. The simulations were repeated six times using different random seeds, each time with N_{WT} being equal to 200.

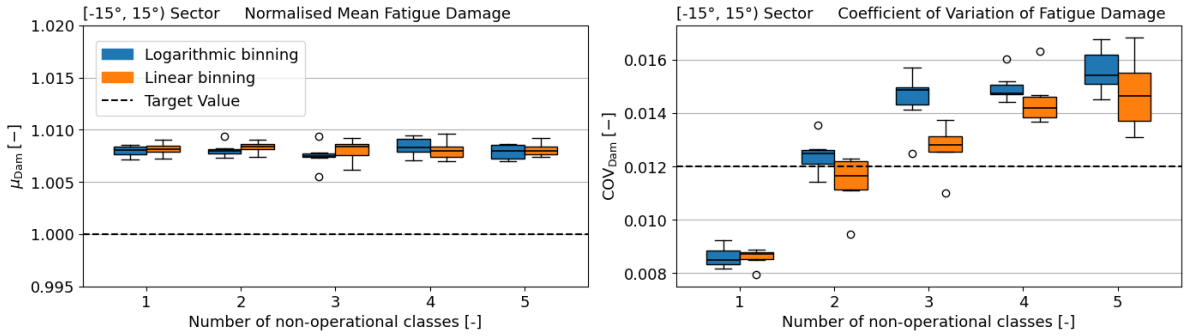

Figure 4.3: Influence of different number of non-operational classes and binning strategies on mean fatigue damage and COV across 6 seeds for the $[-15°, 15°)$ sector, all sectors can be found in Appendix C.

The graph on the left indicates that the simulated mean fatigue damage is predicted to be higher than what is observed in the control group, regardless of binning strategy or number of non-operational classes, reasons for this discrepancy will be discussed in Chapter 5. In contrast, the right-side graph reveals a clear difference in COV_{Dam} between strategies. As the number of non-operational classes increases, the COV_{Dam} tends to rise, particularly for the logarithmic binning. The same trend for both the mean and COV of fatigue damage is also observed for other sectors, shown in Appendix C. In some sectors, regardless of the number of non-operational classes and/or binning strategy, the COV_{Dam} increases, but not sufficiently to match the observed COV in fatigue damage.

4.2.2. Influence of Number of Non-Operational Classes on Mean and Standard Deviation of Non-Operational Duration

Figure 4.4 illustrates the influence of the number of non-operational classes on the average time spent in the non-operational state and the standard deviation of non-operational durations. The standard deviation of non-operational duration increases with the number of non-operational classes. Thus, with more non-operational classes the model appears to better represent the rare long duration non-operational periods presented in the SCADA data. However, with more non-operational classes the differences between different simulations also increases, more non-operational classes makes the model more unstable and requires a higher N_{WT}.Figure 4.3 also shows that adding more non-operational classes, the difference in COV_{Dam} between simulations tends to increase.

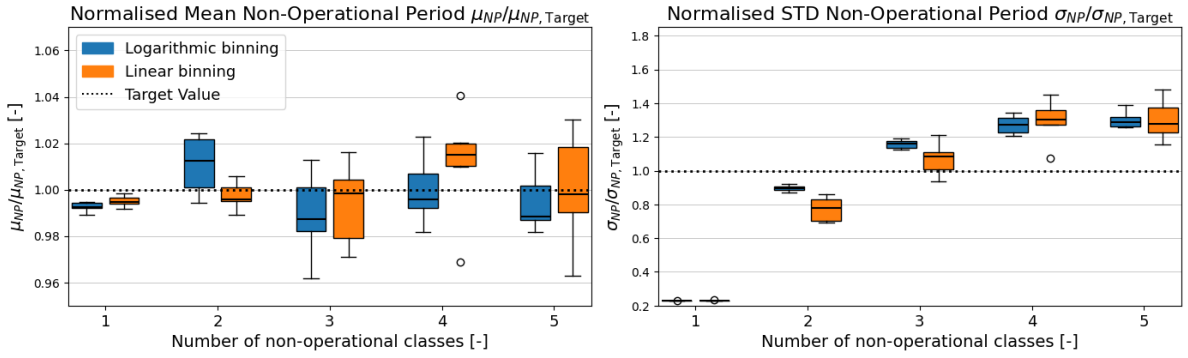

Figure 4.4: Influence of different number of non-operational classes and binning strategies on mean and standard deviation of non-operational durations.

4.2.3. Influence of Number of Non-Operational Classes on Unavailability Error

Figure 4.5 shows the unavailability error, defined as the deviation between the simulated and target ratios of operationality. A value of 1 corresponds to a turbine being entirely non-operational.

With more non-operational classes, it becomes increasingly difficult to match U_{target} exactly, as reflected by the larger spread in Figure 4.5. Both linear and logarithmic non-operational period classification strategies lead to skewness in the resulting error distribution, but the effect is particularly pronounced for the linear strategy. Note that the error magnitude reduces when simulations are extended to a full design life, as statistical fluctuations average out over longer time periods. For example, for logarithmic classification with two non-operational classes, the maximum error in unavailability was 0.015 over the full design life, compared to 0.028 over the SCADA period of 4.5 years on which the calibration was applied.

The underlying reason for the increasing variance and skewness in unavailability error with a higher number of non-operational classes is that increasing the number of non-operational classes improves the representation of long downtime periods. Although such long-duration outages do occur in reality, they are relatively rare and may only be represented a few times throughout the design life. When they occur in the simulation, they have a considerable effect on the resulting availability. This leads to greater variance and skewness in the error distribution, with linear classification amplifying this effect more strongly than logarithmic binning.

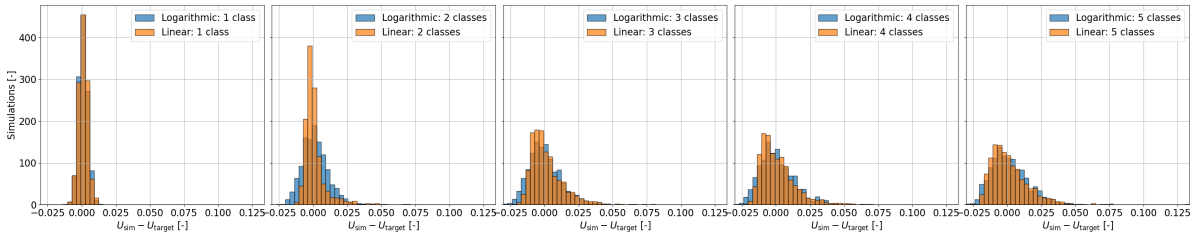

Figure 4.5: Difference between simulated unavailability U_{sim} and long-term theoretical availability U_{target} for different numbers of non-operational classes and binning strategies.

4.3. Final Model Configuration and Performance

Based on the observations in the above section, it was determined that the use of more than two non-operational classes introduces excessive error between the target unavailability and the simulated unavailability. Furthermore, two non-operational classes provided a COV in fatigue damage that was not less than the observed COV in fatigue damage in the $[-15°, 15°]$ sector, the driving sector. However, in other sectors it was observed that two non-operational classes tended to either underpredict or overpredict the observed COV_{Dam}. Using two categories for classifying non-operational periods is also in accordance with [46], where the authors categorised component failures into two different categories. The boundary between these classes was set at 6 hours, as this value best matched the observed COV of the fatigue damage in the driving sector. The transition rates used in the final model are shown in Table 4.2.

Table 4.2: Scaled non-operational transition rates per non-operational class for 5.5% target unavailability.

Non-operational class	λ_{day} [-]	μ_{day} [-]	lower limit [h]	upper limit [h]
1	0.298	18.1	0	6
2	0.0377	0.904	6	∞

The transition rates were adjusted by a correction factor C. In Figure 4.6 the influence of the correction factor C on overall turbine availability is shown, together with the unavailability due to the two different classes of non-operational durations. The correction factor C is defined as 1 for an unavailability ratio of 5.5%, the mean of the used unavailability ratio distribution.

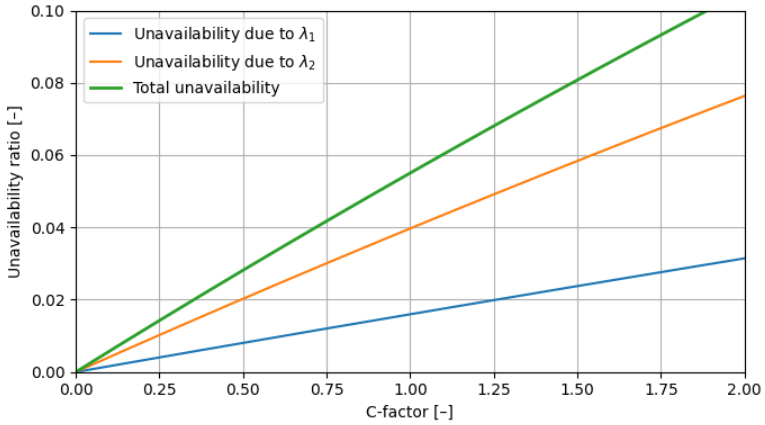

Figure 4.6: Influence of correction factor C to match the long-term theoretical unavailability with the sampled target unavailability.

By using a constant correction factor C for both non-operational classes to scale the long-term unavailability, the ratio between short and long non-operational durations stays constant.

In Figure 4.7 the model performance together with the observed fatigue damage variance is shown. All values are normalised with respect to the fatigue damage obtained by following the 90%/10% operational/non-operational recommended practice of DNV, which is called: Deterministic method. The model over predicts the mean fatigue damage and also the fatigue damage variance is over predicted for this sector. In Table 4.3, the performance of the model for all sectors is summarised. As one can see the model is especially overestimating the mean fatigue damage and the fatigue damage variance in the $[105°, 135°)$, $[135°, 165°)$, while it accurately captures the general trend per sector. The results for all sectors can be found in Appendix D.

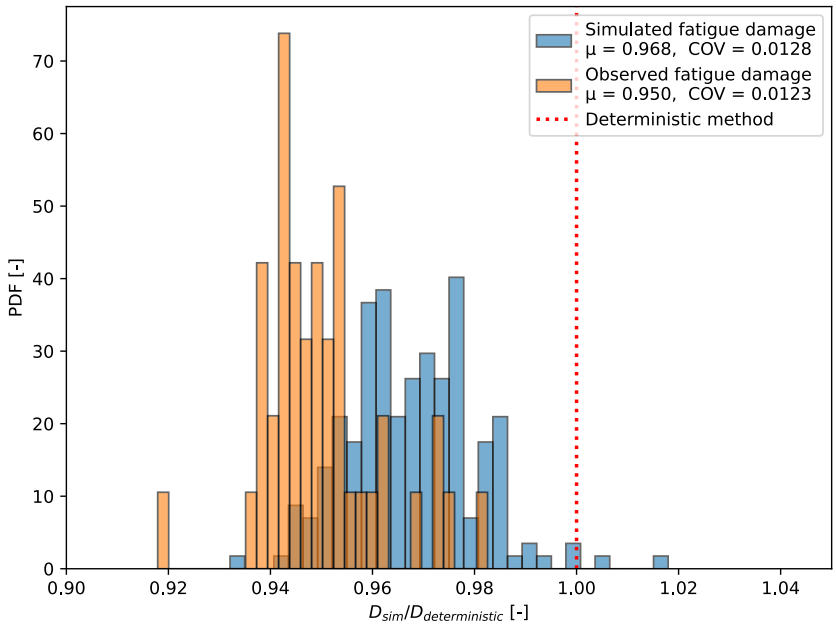

Figure 4.7: Final model performance for the driving sector at mudline in comparison with the observed fatigue damage variance obtained from SCADA data.

It shows that the current DNV approach of assuming a 90%/10% operational/non-operational ratio remains conservative for an 8 MW turbine.

Table 4.3 shows the fatigue damage mean and COV that were obtained by using the availability pat-

terns from the SCADA data and the results produced by the final, calibrated availability model. All mean fatigue damage values are normalised to those obtained using the recommended DNV practice of assuming a 90%/10% operational/non-operational split. The availability model over predicts mean fatigue damage in all sectors. In the $[105°, 135°)$ and $[135°, 165°)$ sectors, the over prediction is substantially larger than in other sectors, the model also overestimates the COV_{Dam} in these sectors more than in other sectors.

Table 4.3: Sector-wise calibration targets: observed vs. final model.

Sector	μ_{Dam}		COV_{Dam}	
	Observed	Final model	Observed	Final model
$[-15°, 15°)$	0.950	0.968	0.0123	0.0128
$[15°, 45°)$	0.993	0.993	0.0113	0.0106
$[45°, 75°)$	0.968	0.976	0.0167	0.0179
$[75°, 105°)$	0.956	0.969	0.0135	0.0131
$[105°, 135°)$	0.886	0.915	0.0210	0.0325
$[135°, 165°)$	0.850	0.907	0.0251	0.0365

Relative to the SCADA data reference, the model over predicts the mean non-operational duration, as the normalised mean was equal to 1.03. The model under predicts the standard deviation of non-operational periods, as the normalised standard deviation was equal to 0.72, meaning it under-represents long non-operational durations.

4.4. Full Design Life Simulations

The final availability model is now used to predict the variance of fatigue damage for two different turbine sizes. The same metocean dataset is applied across both turbine sizes, covering a 25-year span. For this the number of iterations per simulation, N_{WT}, is reduced from 200 to 100, due to computational constraints.

All results are normalised against the damages per sector obtained by following the recommended 90% operational and 10% non-operational practice of DNV, as explained in Section 2.2.2. By doing this, one can test the validity of this practice for a smaller and larger sized turbine and control if this practice is still conservative for both sizes of turbines.

Figure 4.8 illustrates the variance in fatigue damage for the 8 MW turbine model in the $[-15°, 15°)$ sector. Figure 4.8a illustrates the fatigue damage accumulation over the design life. The turbines with maximum and minimum fatigue damage are indicated, while all other turbines are represented within the blue range. The dotted red line indicates the damage obtained when performing the recommended DNV practice, and all fatigue damages are normalized to this value. The orange dotted line illustrates perfect linear fatigue damage accumulation as a reference.

Figure 4.8b shows the resulting fatigue damage distribution at the end of the design life. All turbines fall between 95% and 99% of the fatigue damage compared to the fatigue damage obtained using the recommended DNV approach. The turbines' unavailability is modelled by a beta distribution bounded between 4% and 10%, with a mean of 5.5% and a standard deviation of 1%. The results of all sectors can be found in Appendix E.

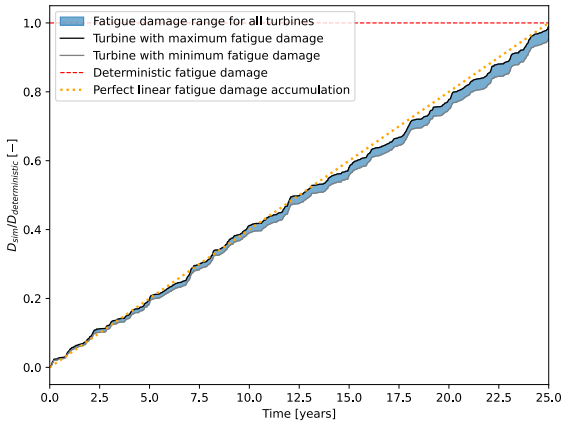

(a) Accumulation of fatigue damage in the driving sector $[-15°, 15°)$. The blue shaded range encloses the turbines with minimum and maximum damage, the dashed red line marks the deterministic fatigue damage level used for normalisation, and the orange dotted line represents perfect linear fatigue damage accumulation.

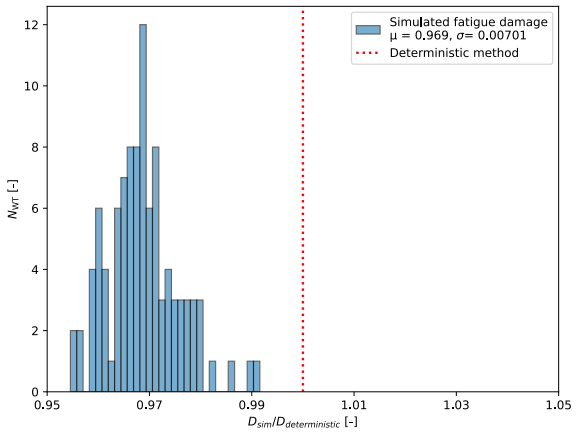

(b) Histogram of fatigue damage per turbine simulated in the driving sector after 25-year design life. The vertical dashed red line indicates the deterministic fatigue damage level.

Figure 4.8: Predicted fatigue damage for the 8 MW turbine at mudline in the driving sector $[-15°, 15°)$. Figure (a) Development of fatigue damage over the full 25-year design life. Figure (b) Distribution of the resulting fatigue damage at the end of the design life. In both figures all values are normalised with respect to the deterministic method (90% operational / 10% non-operational) recommended by DNV.

When performing the same simulations for the 14 MW turbine model, the results obtained are shown in Figure 4.9, which illustrates the fatigue damage accumulation for the 14 MW turbine model. Figure 4.9a shows the fatigue damage accumulation over the design life, while Figure 4.9b presents the resulting fatigue damage distribution at the end of the design life. As observed, the mean fatigue damage is now equal to 1.0, even with a mean non-operational ratio of 5.5%. Note that a fatigue damage value of 1.0 represents the damage obtained by following the DNV approach, which assumes a ratio of 90% operational and 10% non-operational periods. The variance in fatigue damage also increases for the 14 MW turbine when compared to the 8 MW model.

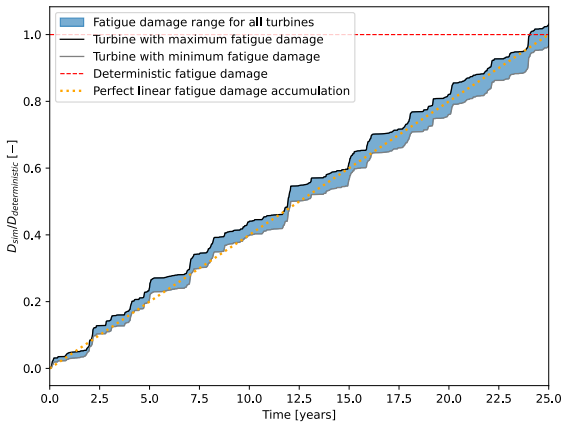

(a) Fatigue damage accumulation over the design life in the driving sector $[-15°, 15°)$. The blue shaded range encloses the turbines with minimum and maximum damage, the dashed red line marks the deterministic fatigue damage level used for normalisation, and the orange dotted line represents perfect linear fatigue damage accumulation.

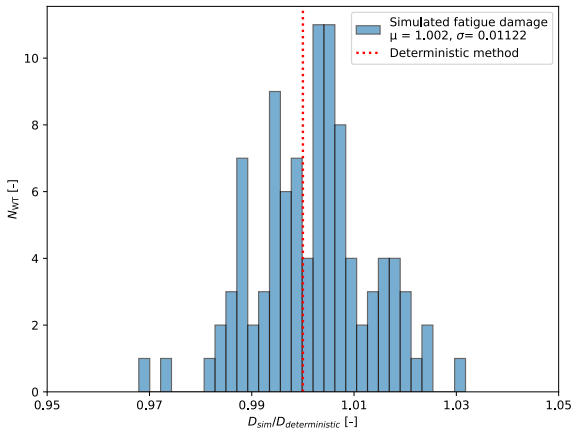

(b) Histogram of fatigue damage per turbine simulated in the driving sector after 25-year design life. The vertical dashed red line indicates the deterministic fatigue damage level.

Figure 4.9: Predicted fatigue damage for the 14 MW turbine at mudline in the driving sector $[-15°, 15°)$. Figure (a) Development of fatigue damage over the full 25-year design life. Figure (b) Distribution of the resulting fatigue damage at end of design life. In both figures all values are normalised with respect to the deterministic method (90% operational / 10% non-operational) recommended by DNV.

Comparing Figure 4.8a and Figure 4.9a shows that the 14 MW turbine experiences more intensive fatigue damage events than the 8 MW turbine. For example, around t=12 years, a sharp increase in fatigue damage is observed. This increase occurs for both turbines, but for the 14 MW turbine this increase is more pronounced than for the 8 MW turbine. After inspection of the metocean conditions for that time period it was found that it was not due to a single or couple events, but rather an unusual harsh winter environment, characterised by sustained high significant wave heights over a longer period compared to other winters in the dataset

5

Discussion

In this chapter the most important outcomes of the results are summarised and placed within the context of current offshore wind turbine design methodologies. In Section 5.2, the influence of the chosen unavailability ratio on fatigue damage variance is evaluated. In Section 5.3, reasons for the availability model to over predict the mean fatigue damage will be presented. Finally, limitations and shortcomings of the current model are discussed together with recommendations to improve the model.

5.1. Implications for Offshore Wind Turbine Design Standards

The results in Section 4.4 show higher fatigue damage variance for larger turbines due to operational variances at the studied site. Current design methods, described by IEC standards and DNV guidelines, are based on mean fatigue damage during non-operational periods from long-term hindcasts and do not include this variance. For the 8 MW turbine, the 90%/10% operational/non-operational split recommended by DNV was still conservative. This was also concluded in [35] for the DTU 10 MW reference turbine. However, for the 14 MW turbine, the availability model showed a 40% increase in fatigue damage variance w.r.t. the 8 MW model and a higher mean fatigue damage in the driving sector. These findings suggest that the current 90%/10% recommendation and the practice of using the the full hindcast for the non-operational FLS DLC may be non-conservative.

Nevertheless, the fatigue damage variance of the 14 MW turbine in the case study was small in absolute terms. In the drivinf sector a fatigue damage COV of approximately 1.1% was observed and a maximum of 4.9% across all sectors. It should be noted that for the 8 MW model, comparison with SCADA-based availability patterns showed that the variance and mean were significantly overpredicted in this maximum-COV sector.

The sectoral differences in fatigue damage variance can be understood by examining the metocean conditions, presented in Appendix B, and the raw frequency-domain simulations. Because, for the site considered, wave incidence is predominantly from the North, the $[-15°, 15°)$ sector is the driving direction.

This sector also shows the lowest variance. This can be linked to the relatively low spread in the ratio of non-operational to operational fatigue damage in that sector. By contrast, other sectors display substantially higher fatigue damage variance (see Appendix E), reflecting larger fluctuations in this ratio driven by fatigue damage intensive events in these sectors. It is therefore somewhat fortunate that, for the site considered, the sector with the highest fatigue damage variance, does not coincide with the dominant loading direction. At other sites, however, alignment of the driving and high-fatigue damage variance sectors could significantly amplify uncertainty in fatigue damage predictions.

To place these variances, or uncertainties, in perspective, it is useful to compare them with other sources of uncertainty considered in current design practices and reliability engineering. For instance, load model uncertainties such as X_{wave} are typically represented with a COV of around 10% [29]. This indicates that, although the contribution from wave loading variance due to operational variances, for the site considered, is smaller than uncertainties already accounted for in reliability-based calibrations of PSF, it still represents an additional source of uncertainty which is currently not accounted for and shows that fatigue life predictions are: (i) Sensitive to the way operational availability is represented in

current DLCs approaches. (ii) The fatigue damage variance is increasing for larger turbines.

The relatively small absolute increase in fatigue damage variance when moving from the 8 MW to the 14 MW turbine model can also be explained by the persistence of fatigue-critical resonant sea states. As shown in Figure 5.1, these sea states, with peak periods T_p close to the natural frequencies, are still common in the metocean climate of the case study site. As a result, their contribution is well represented over the lifetime, keeping the overall fatigue damage variance relatively small. For future, lower natural frequency, monopile-based offshore wind turbines, the variance in fatigue damage due to operational variances could increase rapidly. This can be seen in Figure 5.1, fatigue-critical resonant sea states will become increasingly rare once the natural frequency drops below approximately 0.15 Hz at the site considered in this thesis. At the same time, the potential impact of these resonant conditions becomes more pronounced, since their occurrence coincides with larger significant wave heights, resulting in an increased contribution to the total fatigue damage.

Note that the natural frequencies shown in Figure 5.1 correspond to publicly available reference turbines. The actual natural frequencies of the case study turbines cannot be disclosed due to confidentiality. These reference values are included to illustrate the trend between turbine natural frequency and the T_p distribution.

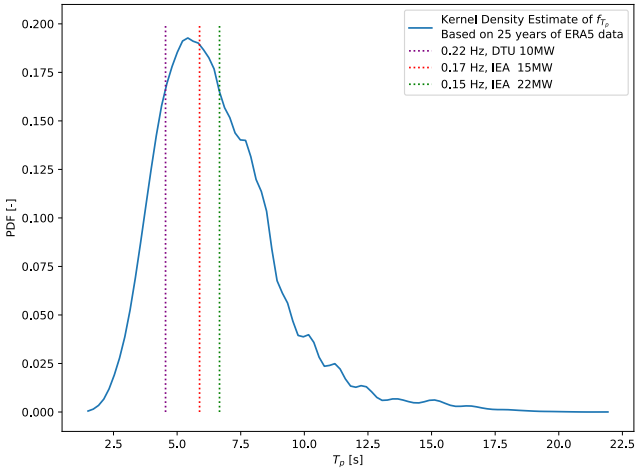

Figure 5.1: Kernel Density Estimate of the f_{T_p} probability density function and natural frequencies of reference turbines. The figure illustrates the rapid decrease in the probability of occurrence of fatigue-critical resonant sea states as natural frequency decreases. Note that the figure does not account for the additional increase in fatigue damage associated with higher significant wave heights at larger T_p values.

It should be emphasised that uncertainty from wave loading variance could be highly site-specific. At deeper, more wave-driven offshore sites, wave-induced fatigue damage variance due to operational variances may be higher. This is because wave steepness limits at such sites can be less restrictive, allowing sea states with larger significant wave heights at lower peak periods. Similarly, the peak of the T_p marginal distribution may shift leftward, making resonant sea states less prevalent in the hindcast and potentially increasing fatigue damage variance. Finally, extreme sea states may also occur more often and with greater variance in their significant wave height at other locations, further increasing fatigue damage variance.

To account for this uncertainty, methodologies could adopt more probabilistic treatments of operational availability or apply deterministic approaches with site-specific calibrated PSFs that fully capture site-specific variances in wave conditions. This aligns with [41], which also emphasises the need for site-specific partial safety factors but for the reason to address location-dependent effects of climate change on wave conditions. Climate change not only shifts mean wind and wave characteristics but can also amplify their variability and extremes [48], which in turn could further amplify fatigue damage variance due to variances in operational availability. In line with this, [49] showed that fatigue damage for a 22 MW monopile-based turbine increased by 17% (tower) and 11% (monopile) under RCP4.5 (a moderate-emission climate scenario), and by 52% (for both the tower and monopile) under RCP8.5

(a high-emission climate scenario), compared to historical hindcast data. These results highlight that relying on current DLC practices, together with generic, non site-specific, PSFs only focused on model uncertainties, and both based on historical hindcasts, may become increasingly non-conservative for next-generation offshore wind turbines.

An additional consideration is the role of hydrodynamic load model uncertainty. Linear wave theory, which assumes small wave steepness, and the Morison equation under slender-body conditions (see Section 2.3.1), become less accurate in near-resonance, high-H_s storm conditions that are increasingly important for fatigue damage in larger monopile-based turbines. In [50], the authors showed that including second-order wave effects can reduce predicted design lifetimes by several years and introduce sea-state-dependent model uncertainty.

To address this, load model uncertainties should not be treated uniformly but weighted by both the relative fatigue contribution of each sea state and their corresponding sea-state-specific model uncertainty, ensuring that the dominant fatigue-driving conditions, and their uncertainties, are properly reflected in fatigue life predictions.

5.2. Influence of Higher Variance in Unavailability Ratios

The results presented in Section 4.4 adopted a conservative basis by applying the 90%/10% operational/non-operational recommendation from DNV, whereas many current offshore wind turbine designs assume a smaller non-operational ratio. Furthermore, the unavailability ratio PDF used provided a conservative estimate by being bounded between 4% and 10%. For comparison, [35] applied a beta distribution defined over the full range from 0 to 1, without imposing such bounds. This section will show the effect of not imposing bounds on the unavailability ratio distribution.

The results in Section 4.4 were obtained using an unavailability ratio PDF bounded between 4% and 10%, thereby focusing on as-expected turbine behaviour. When this assumption is relaxed to account for turbines that experience major faults, and thus can remain non-operational for longer periods, the boundaries must be widened. By using the unavailability ratio shown in Figure 5.2, one can determine the fatigue damage variance and show the influence of the relaxed assumption.

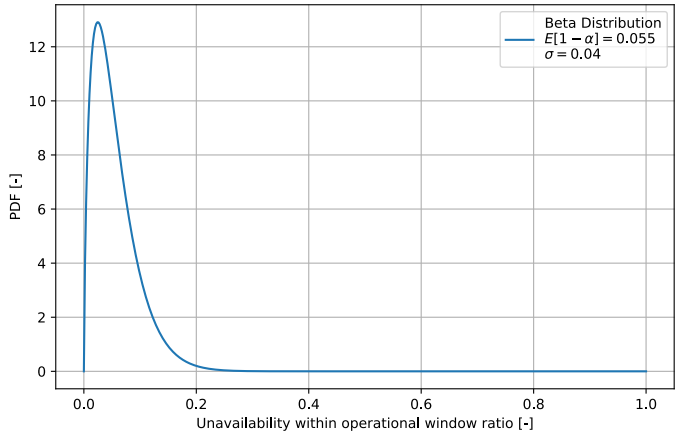

Figure 5.2: Unbounded beta distribution used for representing unavailability ratio within the operational window that is between 0% and 100%. With a mean unavailability of 5.5% and standard deviation of 4%.

By following the same procedure to simulate the fatigue damage variance as outlined in Section 4.4, for the 8 MW model, the results shown in Figure 5.3 are obtained. As illustrated in Figure 5.3a, the fatigue damage variance increases. Notably, now also for the 8 MW turbine model, some turbines exhibit higher fatigue damage than what would be expected when following the recommended DNV approach (the red dotted line), while the mean fatigue damage is not influenced. The results for all sectors are shown in Appendix F. The variance in fatigue damage increased significantly for the $[105°, 135°)$ and

$[135°, 165°)$ sector. It must be noted that for these sectors the model already tended to over predict the fatigue damage variance when compared to the fatigue damage variance obtained from matching the SCADA data availability profiles with frequency domain simulations.

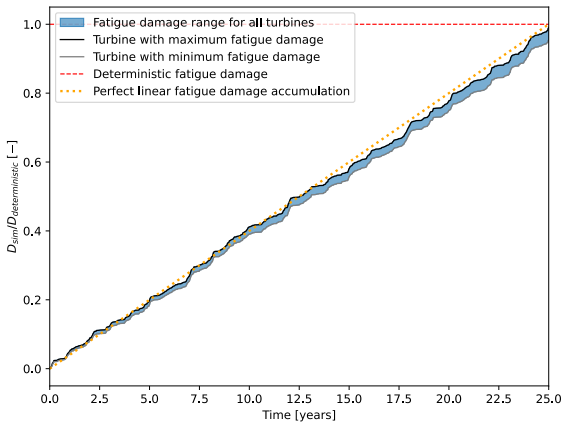

(a) Accumulation of fatigue damage in the driving sector $[-15°, 15°)$. The blue shaded range encloses the turbines with minimum and maximum fatigue damage, the dashed red line marks the deterministic fatigue damage level used for normalisation, and the orange dotted line represents perfect linear accumulation.

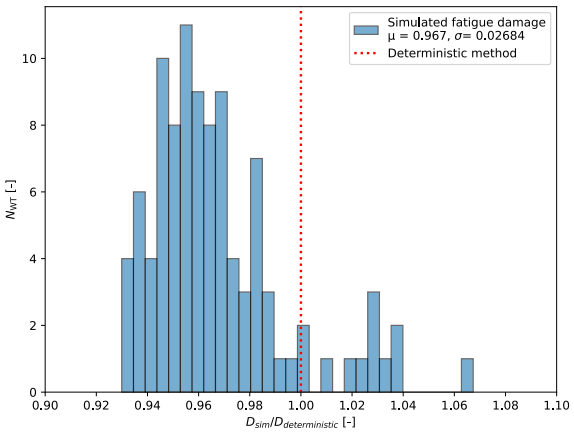

(b) Histogram of fatigue damage per turbine simulated in the driving sector after 25-year design life. The vertical dashed red line indicates the deterministic fatigue damage level.

Figure 5.3: Predicted fatigue damage at mudline for the 8 MW turbine in the driving sector $[-15°, 15°)$, with a relaxed unavailability ratio PDF. Figure (a) Development of fatigue damage over the full 25-year design life. Figure (b) Distribution of the resulting fatigue damage at the end of the design life. In both figures all values are normalised with respect to the deterministic method (90% operational / 10% non-operational) recommended by DNV.

However, when the unavailability ratio PDF shown in Figure 5.2 is applied to the 14 MW turbine and compared with the 8 MW model, the increase in fatigue damage variance in the driving sector $[-15°, 15°)$ is less pronounced than for the 8 MW turbine. For the other sectors, shown in Appendix F, a larger increase in fatigue damage COV is observed, although the relative increase remains consistently larger for the 8 MW model in all sectors except $[45°, 75°)$. In absolute terms, the 8 MW model exhibits a larger variance increase in the driving sector, whereas in all other sectors the absolute increase in fatigue damage variance is higher for the 14 MW model.

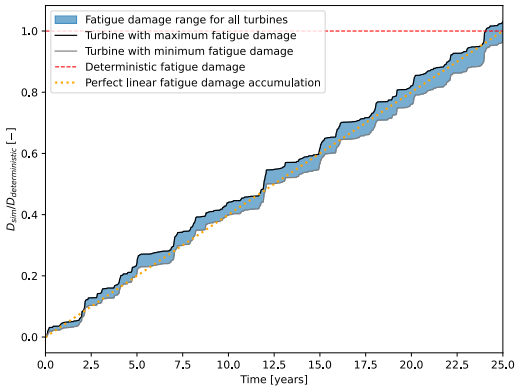

(a) Accumulation of fatigue damage in the driving sector $[-15°, 15°)$ when the unavailability ratio is not bounded between 4% and 10%. The blue shaded range encloses the turbines with minimum and maximum damage, the dashed red line marks the deterministic fatigue damage level used for normalisation, and the orange dotted line represents perfect linear accumulation.

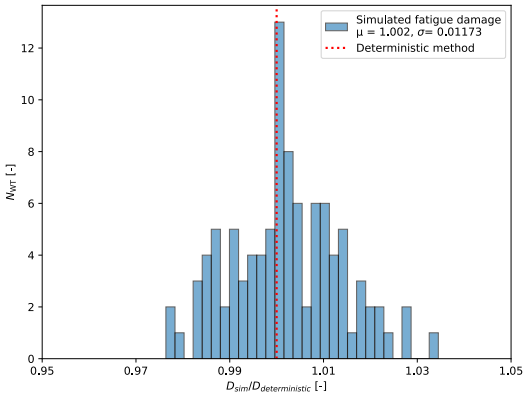

(b) Histogram of fatigue damage per turbine simulated in the driving sector after 25-year design life. The vertical dashed red line indicates the deterministic fatigue damage level.

Figure 5.4: Predicted fatigue damage at mudline for the 14 MW turbine in the driving sector $[-15°, 15°)$, with a relaxed unavailability ratio PDF. Figure (a) Development of fatigue damage over the full 25-year design life. Figure (b) Distribution of the resulting fatigue damage at the end of the design life. In both figures all values are normalised with respect to the deterministic method (90% operational / 10% non-operational) recommended by DNV.

Although the normalisation of results prevents a direct comparison of magnitudes across sectors, it is noteworthy that for the 14 MW model the elevated fatigue damage variance in the $[135°, 165°)$ sector was sufficient to shift the dominant fatigue contribution in some iterations, making this sector the effective driving sector instead of the $[-15°, 15°)$ sector, which would normally be assumed to be the driving sector under the current deterministic design methods.

5.3. Limitations of the Availability Model

The framework for the current method of modelling availability-variance-induced fatigue damage variance has various shortcomings. One key shortcoming was the relatively low number of iterations per simulation. With only 100 iterations, the model could fail to capture important outliers in fatigue damage caused by rare fatigue-critical sea states. Another key limitation was the deviation in predicted mean fatigue damage between the simulations and the SCADA-observed availability profiles.

A methodological limitation is that the operational wind speed windows used for the 8 MW and 14 MW models were not identical, which may have influenced the comparative results. Moreover, in theory widening the operational wind speed window has the potential to increase fatigue damage variance: wind speeds that are currently beyond cut-out (and thus always parked) would become conditions under which the turbine may or may not be operating. To the authors' knowledge, no published literature explicitly identifies this as a possible downside of widening the operational wind speed window. Various other limitations of the current method of modelling availability-variance-induced fatigue damage variance and ways to improve the availability model shortcomings will be discussed in the following section.

5.3.1. Uniform Transition Probability Assumption

The present modelling framework assumes that the probability of a turbine transitioning from and to non-operational state is (i) constant throughout its design life, and (ii) independent of both the metocean conditions and any prior faults. As pointed out in [45], the original paper describing the used availability model, this simplification can be accounted for by introducing time-dependent failure rates (e.g., bathtub curves) for individual components. Doing so would allow the model to capture early-life "infant mortality", a period of relatively stable operation, and the wear-out phase near end-of-life. This could also be incorporated for the model proposed in this thesis by adjusting the probabilities of going into non-operational state with a bathtub-curve.

Another assumption is that the transition probability from operational to non-operational state is uniform for all environmental conditions. However, after analysing SCADA data it revealed that this uniformity assumption is not valid. Figure 5.5 illustrates this point. In the figure, the wind speed is discretised into bins with a width of 1 m/s. For each bin, the relative representation between the operational and non-operational states is calculated, where a ratio of 1 indicates that a wind speed bin is represented equally often in both states. As can be seen, wind speeds between approximately 9 m/s and 23 m/s are under-represented in the non-operational states compared with the operational state (ratio < 1). In other words, turbines are less likely to shut down at moderate wind speeds than the model prescribes. Conversely, lower (≤ 8 m/s) and higher (≥ 23 m/s) wind speeds are relatively over-represented in the non-operational state (ratio > 1).

This difference in relative occurrence can be attributed to various reasons. For example, the current model does not differentiate between non-operational periods due to maintenance or non-operational periods due to faults. As maintenance is only carried out during favourable weather conditions and faults can occur anytime.

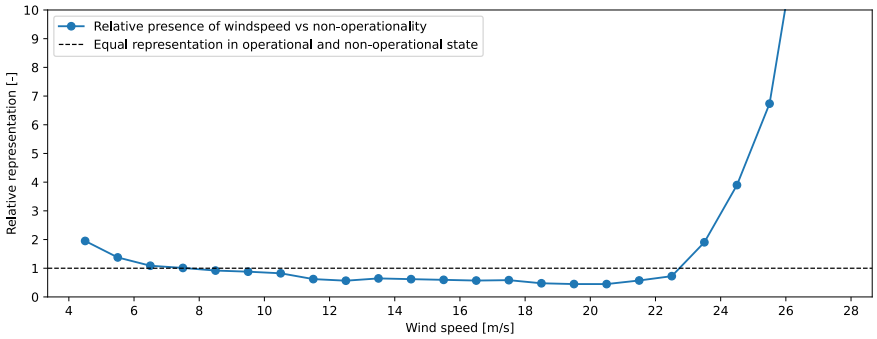

Figure 5.5: SCADA data retrieved relative representation of operational state vs. non-operational state across the operational wind speed window (4–28 m/s).

5.3.2. Uniform Wind Speed Assumption

Another assumption is the uniform wind speed for all wind turbines. Treating the metocean conditions as homogeneous allowed all measurements to be merged into a single dataset and reduced the computational effort required for modelling the DELs per metocean condition. However, this comes at the cost of ignoring intra-farm wind speed deviations. Neglecting these variations removes turbine-specific availability profiles for the non-operational state when the wind speed falls outside the operational wind speed window. This limitation is illustrated in Figure 5.6, where SCADA data were normalised with the farm-wide mean to highlight relative differences. The figure shows that some turbines experienced around 10% more, while others experienced around 10% less, occurrences of wind speeds outside the operational wind speed window compared to the wind farm average.

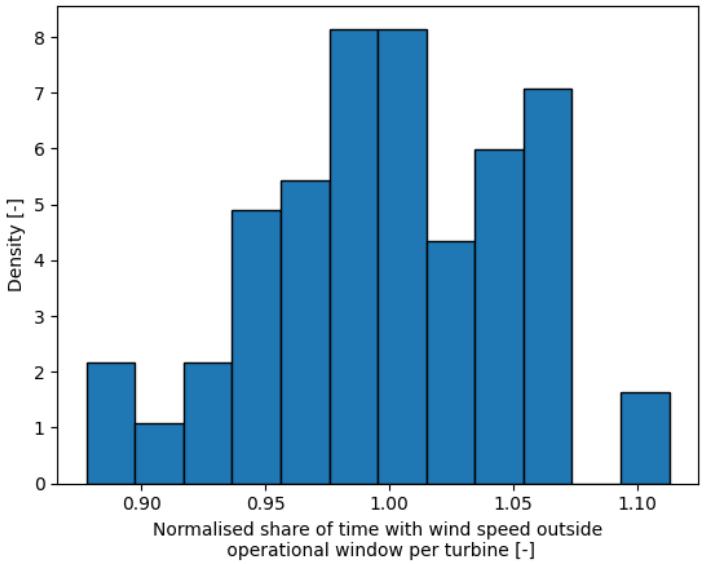

Figure 5.6: Normalised occurrence of State 3 (wind speeds outside the operational window) derived from SCADA data, values are scaled so that the mean equals 1.0.

The variance in fatigue damage predicted by the model is close to what is inferred from SCADA-based availability profiles for four out of six sectors. Yet the turbine-to-turbine differences in out-of-window periods seen in the SCADA data are not captured, since the model treats these periods as identical across turbines. As a result, the model assigns too much of the variance to non-operational periods within the operational wind speed window, leading to an over prediction of fatigue damage variance caused by non-operational periods within the operational wind speed window. This may be implicitly compensated by assuming no turbine-to-turbine variance in out-of-window periods, but the SCADA

availability profiles benchmark used to calibrate the model already contains wake effects and their influence on availability.

5.3.3. Scaling of Non-Operational Transition Probabilities

The current availability model scales all transition probabilities to non-operational classes, λ_i, constantly. By doing so, the ratio between short and long non-operational periods remains fixed. However, when a turbine is non-operational for a longer time, it is more likely due to a severe, long-lasting downtime rather than multiple short interruptions, which is not reflected in the current model. Moreover, the μ_i parameters are not scaled but treated as constant. If, instead, the μ_i parameters were adjusted, the availability model could better capture the long non-operational periods that are present in the SCADA data.

5.3.4. Metocean Data Limitation

The current availability model relies on a 25-year metocean dataset. However, rare fatigue-critical sea states may be under-represented in such a limited time window, and a different 25-year subset could yield different results. This introduces additional uncertainty in fatigue damage predictions that is not explicitly accounted for in the availability model developed in this thesis. In [35], this limitation was addressed by sampling from a long-term joint distribution of metocean conditions using a Gibbs sampling approach. However, their analysis focused primarily on the parked (faulted) and operational sub-populations, as these dominated the fatigue damage contributions in their case.

As a result, variance in storm-driven conditions between one design life (taken in this thesis as 25 years) subset and another was not captured, even though such events may become increasingly important for larger turbines with lower natural frequencies.

6

Conclusions and Recommendations

This thesis set out to evaluate how turbine-to-turbine availability variance influences the fatigue design life of monopile-based offshore wind turbines. This was done by adapting an existing Markov-based availability model, described in [45], to be SCADA-driven. Observed turbine availability patterns were combined with frequency-domain simulations to assess the influence of availability variance on fatigue damage over the full design life.

The main conclusion is that availability-driven variance introduces an additional source of uncertainty. While relatively small for the studied site compared to uncertainties already accounted for in PSFs calibration, this effect increases with turbine size and is not currently reflected in PSFs calibration methods. Availability-induced fatigue damage variance may also be site-specific, since the ratio of fatigue damage between operational and non-operational periods, and its spread across sea states, is influenced by the local metocean climate.

The results therefore justify the need for site-calibrated PSFs, as has also been suggested in the context of climate-change-driven shifts in wave loads and wave climate [41], or, alternatively, more probabilistic design approaches.

The current design methods to evaluate the FLS for offshore wind turbine support structures are based on simulations of different DLCs, in which discretised long-term hindcasts are used to represent environmental loading. With the increase in turbine size over the last decade, natural frequencies have decreased, shifting fatigue-critical, near-resonant sea states from commonly occurring conditions toward rarer, (near-)resonance high-H_s storm events.

As a result, fatigue damage is therefore increasingly more concentrated in short time windows, particularly during non-operational periods when aerodynamic damping is low. This implies that current design methods, which rely on long-term hindcasts and mean fatigue damage assumptions, may underestimate the contribution of these rare fatigue-critical conditions during non-operational periods to fatigue life.

This thesis has therefore focused on quantifying how turbine-to-turbine availability variance influences fatigue life predictions when compared with current deterministic design practice. The adapted SCADA-driven availability model was applied to two turbine sizes, 8 MW and 14 MW, to test the adequacy of the DNV recommendation of a fixed availability ratio of 90%/10% operational/non-operational. In doing so, it enabled an assessment of the adequacy of current design methodologies.

To achieve this, the SCADA dataset was first divided using a 50/50 train–test split: transition probabilities were estimated from the training set and then used to simulate availability, which were compared against the SCADA data availability profiles in the test set. This validation showed that the adapted availability model reproduced the driving-sector behaviour reasonably well, but tended to overpredict mean fatigue damage and its variance in several other sectors.

These estimated transition rates were then used to generate full design-life simulations and corresponding fatigue damage predictions. To represent downtime stochastically, non-operational ratios were represented using a beta distribution with a mean non-operational fraction of 5.5%. Importantly, the results indicate that the conventional assumption of a deterministic 90%/10% operational/non-operational split

remains conservative for the 8 MW turbine, in line with [35], who argued that modelling non-operational periods stochastically could reduce conservatism. By contrast, for the 14 MW turbine, absolute fatigue-damage variance was small for the site studied (driving-sector fatigue damage COV ≈ 1.1%, up to 4.9% in other sectors), but full-life simulations indicate that in some cases fatigue damage predicted using the availability model can exceed the deterministic 90%/10% DNV recommendation, corresponding to an increase of about 3% in total fatigue damage relative to that predicted under the deterministic 90%/10% DNV recommendation.

Therefore, for larger turbines, the results suggest that stochastic modelling of non-operational periods may not reduce conservatism, but could be required to avoid non-conservatism. However, the extent of this effect is expected to be site-dependent. It should also be emphasised that the availability model tended to overpredict mean fatigue damage and variance during validation against SCADA data availability profiles for the 8 MW turbine model, which means that the degree of potential non-conservatism indicated here may be overestimated.

Several important limitations should be noted with these conclusions. First, the availability model depends on a 25-year metocean hindcast; rare, fatigue-critical storm states may be underrepresented in such a window, and different 25-year subsets can yield different design-life damage estimates. Second, the present model assumes homogeneous, environment-independent transition probabilities and does not capture intra-farm wind-speed deviations. These simplifications affect the partitioning of variance between periods when the wind speed is within the operational window and periods when the wind speed is outside the operational window, leading the model to attribute a too large proportion of the total fatigue damage variance accumulated during non-operational periods within the operational wind speed window.

Furthermore, climate change introduces additional uncertainty. Shifts in the frequency and intensity of rare fatigue-critical events, as well as long-term changes in wave climate, could alter the occurrence of fatigue-critical conditions over a turbine's design life. Consequently, reliance on historical hindcasts alone may not provide a representative basis for reliable fatigue design of future offshore wind farms, and availability-driven variance could be amplified as extreme events increasingly coincide with non-operational periods.

The findings of this thesis therefore highlight the need to revisit assumptions in the non-operational DLC, particularly with respect to availability modelling, and to consider site-specific calibration of PSFs or probabilistic design approaches, so that availability-driven and other site-specific uncertainties are properly reflected in future offshore wind turbine design practice. In support of this, the results show that turbine-to-turbine availability variance, quantified using a SCADA-driven model, influence fatigue life predictions: while the deterministic DNV 90%/10% recommendation remains conservative for smaller turbines at the studied site, it may become non-conservative for larger turbines.

6.1. Recommendations

This thesis provides a basis for developing design methodologies that explicitly account for fatigue damage variance within a wind farm. Future work should therefore focus on:

Improved availability modelling: The availability model should be extended to include non-homogeneous, environment-dependent transition probabilities. Wake effects should be included, since they influence both turbine downtime and the resulting fatigue damage variance. Incorporating real failure rates and subcomponent-level data would further improve realism. In addition, future models should distinguish between downtime caused by faults (random) and downtime caused by maintenance (planned).

Enhanced representation of metocean conditions: Longer hindcast records should be combined with statistically correlated sampling methods (e.g., Gibbs sampling). These methods should not only capture rare, fatigue-critical storm states but also include variance in the amount of time wind speed falls outside the operational window.

Accounting for long-term climate change: Projections of future metocean conditions should be incorporated in the calibration of PSFs, so that potential shifts in the frequency and intensity of extreme storm events, as well as long-term wave climate trends, are reflected in fatigue design.

References

[1] H. Ritchie and P. Rosado. “Fossil fuels,” Our World in Data. (Oct. 2, 2017), [Online]. Available: https://ourworldindata.org/fossil-fuels (accessed on: 03/22/2025).

[2] National Grid Group. “The history of wind energy,” National Grid Group. (), [Online]. Available: https://www.nationalgrid.com/stories/energy-explained/history-wind-energy (accessed on: 02/26/2025).

[3] A. Buljan. “Siemens Gamesa to soon install 21 MW offshore wind turbine prototype at Danish test site - reports,” offshoreWIND.biz. (Dec. 10, 2024), [Online]. Available: https://www.offshorewind.biz/2024/12/10/siemens-gamesa-to-soon-install-21-mw-offshore-wind-turbine-prototype-at-danish-test-site-reports/ (accessed on: 02/26/2025).

[4] London Array. “London Array - a leader in offshore renewable energy since 2013.” (), [Online]. Available: https://londonarray.com/ (accessed on: 02/26/2025).

[5] EnergyNews. “Global offshore wind power on course for 520 GW by 2040, with Europe in the lead.” (Aug. 26, 2024), [Online]. Available: https://energynews.pro/en/global-offshore-wind-power-on-course-for-520-gw-by-2040-with-europe-in-the-lead/ (accessed on: 05/01/2025).

[6] World Forum Offshore Wind, “Global offshore wind report 2024,” Annual report 2024, Apr. 2024. [Online]. Available: https://wfo-global.org/wp-content/uploads/2025/04/WFO_Global-Offshore-Wind-Report-2024_final.pdf (accessed on: 02/26/2025).

[7] Business Norway. “Advantages and disadvantages of offshore wind.” (Sep. 22, 2024), [Online]. Available: https://businessnorway.com/articles/advantages-and-disadvantages-of-offshore-%20wind (accessed on: 03/18/2025).

[8] A. Mariano. “Can the UK become the ’Saudi Arabia of wind power’?” Pager Power. (Oct. 20, 2020), [Online]. Available: https://www.pagerpower.com/news/can-the-uk-become-the-saudi-arabia-of-wind-power/ (accessed on: 05/01/2025).

[9] OX2. “Offshore wind power.” (), [Online]. Available: https://www.ox2.com/what-we-do/solutions/offshore-wind-power/ (accessed on: 03/18/2025).

[10] Ørsted. “Advantages of offshore wind.” (), [Online]. Available: https://us.orsted.com/renewable-energy-solutions/offshore-wind/what-is-offshore-wind-power/advantages-of-offshore-wind (accessed on: 03/18/2025).

[11] M. Shields, P. Beiter, J. Nunemaker, A. Cooperman, and P. Duffy, “Impacts of turbine and plant upsizing on the levelized cost of energy for offshore wind,” *Applied Energy*, vol. 298, p. 117 189, Sep. 15, 2021, ISSN: 0306-2619. DOI: 10.1016/j.apenergy.2021.117189.

[12] J. Jonkman, S. Butterfield, W. Musial, and G. Scott, “Definition of a 5-MW reference wind turbine for offshore system development,” NREL/TP-500-38060, 947422, Feb. 1, 2009, NREL/TP–500–38 060, 947 422. DOI: 10.2172/947422.

[13] E. Gaertner, J. Rinker, L. Sethuraman, F. Zahle, B. Anderson, G. Barter, N. Abbas, F. Meng, P. Bortolotti, W. Skrzypinski, G. Scott, R. Feil, H. Bredmose, K. Dykes, M. Shields, C. Allen, and A. Viselli, “Definition of the IEA 15-megawatt offshore reference wind,” National Renewable Energy Laboratory, Golden, CO, USA, Tech. Rep. NREL/TP-5000-75698, Mar. 2020.

[14] DNV GL AS, *Environmental Conditions and Environmental Loads (DNV-RP-C205)*, Standard, version 2020, Høvik, Norway, Sep. 2019.

[15] Power Engineering International. “LCOE for offshore wind now on par with coal – BNEF,” Power Engineering International. (Jun. 9, 2023), [Online]. Available: https://www.powerengineeringint.com/renewables/lcoe-for-offshore-wind-now-on-par-with-coal-bnef/ (accessed on: 02/26/2025).

[16] K. Carter. “Unearthing rare earths.” (Jul. 15, 2021), [Online]. Available: https://www.windsystemsmag.com/24015-2/ (accessed on: 05/10/2025).

[17] “The wind power industry is facing major cost headwinds. here’s what can be done,” World Economic Forum. (Nov. 23, 2023), [Online]. Available: https://www.weforum.org/stories/2023/11/why-offshore-wind-cost-pressures-rising/ (accessed on: 06/10/2025).

[18] T. York. “Why wind farm developers are pulling out at the last minute,” The Conversation. (Jun. 9, 2025), [Online]. Available: http://theconversation.com/why-wind-farm-developers-are-pulling-out-at-the-last-minute-256842 (accessed on: 06/10/2025).

[19] WindEurope, “Offshore wind in europe: Key trends and statistics in 2019,” WindEurope, 2019, Feb. 2020.

[20] R. Damiani, K. Dykes, and G. Scott, “A comparison study of offshore wind support structures with monopiles and jackets for U.S. waters,” *Journal of Physics: Conference Series*, vol. 753, no. 9, p. 092 003, Sep. 2016, ISSN: 1742-6588. DOI: 10.1088/1742-6596/753/9/092003.

[21] T. Stehly, P. Duffy, and D. M. Hernando, “2022 cost of wind energy review,” National Renewable Energy Laboratory, Golden, CO, USA, NREL/TP-5000-87578, Dec. 2023.

[22] H. Holt. “Deme offshore installs ‘largest ever offshore wind monopile foundations’,” Windpower Monthly. (Jul. 26, 2022), [Online]. Available: https://www.windpowermonthly.com/article/1794112 (accessed on: 06/12/2025).

[23] Empire Engineering, “The Empire Engineering guide to offshore wind foundations,” Empire Engineering, Bristol, UK. [Online]. Available: https://www.empireengineering.co.uk/wp-content/uploads/2021/08/The_Empire_Engineering_Guide_to_Offshore_Wind_Foundations_eBook-1.pdf (accessed on: 05/10/2025).

[24] S. Jindal, U. Rahmanli, M. Aleem, L. Cui, and S. Bhattacharya, “Geotechnical challenges in monopile foundations and performance assessment of current design methodologies,” *Ocean Engineering*, vol. 310, p. 118 469, Oct. 15, 2024. DOI: 10.1016/j.oceaneng.2024.118469.

[25] P. van der Male and J. S. Hoving, “Jacket-based offshore wind turbines – natural frequency guestimation: OE44097 offshore support structures (2023/24 Q3),” Lecture slides, TU Delft, Delft, The Netherlands, 2024.

[26] J. C. Kaimal, J. C. Wyngaard, Y. Izumi, and O. R. Coté, “Spectral characteristics of surface-layer turbulence,” *Quarterly Journal of the Royal Meteorological Society*, vol. 98, no. 417, pp. 563–589, Jul. 1972. DOI: 10.1002/qj.49709841707.

[27] K. Hasselmann, T. P. Barnett, H. Carlson, D. E. Cartwright, K. Enke, J. A. Ewing, H. Gienapp, D. E. Hasselmann, P. Kruseman, A. Meerburg, P. Müller, D. J. Olbers, K. Richter, W. Sell, and H. Walden, “Measurements of wind-wave growth and swell decay during the joint north sea wave project (JONSWAP),” Deutsche Hydrographische Zeitschrift, Reihe A, Nr. 8, Deutsches Hydrographisches Institut, Hamburg, Germany, 1973. [Online]. Available: https://airsea.ucsd.edu/wp-content/uploads/sites/10/2019/10/Jonswap-Hasselmann1973.pdf (accessed on: 06/28/2025).

[28] D. A. Bouzid, S. Bhattacharya, and L. Otsmane, “Assessment of natural frequency of installed offshore wind turbines using nonlinear finite element model considering soil-monopile interaction,” *Journal of Rock Mechanics and Geotechnical Engineering*, vol. 10, no. 2, pp. 333–346, Apr. 2018. DOI: 10.1016/j.jrmge.2017.11.010.

[29] J. Velarde, E. Vanem, C. Kramhøft, and J. D. Sørensen, “Probabilistic analysis of offshore wind turbines under extreme resonant response: Application of environmental contour method,” *Applied Ocean Research*, vol. 93, p. 101 947, Dec. 2019, ISSN: 0141-1187. DOI: 10.1016/j.apor.2019.101947.

[30] W. Njomo-Wandji, A. Natarajan, and N. Dimitrov, “Influence of model parameters on the design of large diameter monopiles for multi-megawatt offshore wind turbines at 50-m water depths,” *Wind Energy*, vol. 23, no. 12, pp. 2181–2197, Dec. 2020. DOI: 10.1002/we.2322.

[31] M. A. Miner, “Cumulative damage in fatigue,” *Journal of Applied Mechanics*, vol. 12, no. 3, A159–A164, Sep. 1945.

[32] Y. Murakami and T. Endō, *The rainflow method in fatigue*. Oxford, UK and Boston, MA, USA: Butterworth-Heinemann, 1992, Tatsuo Endo memorial volume; papers presented at the International Symposium on Fatigue Damage Measurement and Evaluation Under Complex Loadings, Fukuoka, Japan, July 25–26, 1991, supported by ONO SOKKI Co. Ltd., ISBN: 978-0-7506-0504-5.

[33] T. Dirlik, "Application of computers in fatigue analysis," Ph.D. dissertation, University of Warwick, Coventry, UK, Jan. 1985. [Online]. Available: http://webcat.warwick.ac.uk/record=b1445503~S9 (accessed on: 06/14/2025).

[34] M. Seidel, "Wave induced fatigue loads: Insights from frequency domain calculations," *Stahlbau*, vol. 83, no. 8, pp. 535–541, Aug. 2014, ISSN: 0038-9145. DOI: 10.1002/stab.201410184.

[35] J.-T. Horn and B. J. Leira, "Fatigue reliability assessment of offshore wind turbines with stochastic availability," *Reliability Engineering & System Safety*, vol. 191, p. 106 550, Nov. 2019, ISSN: 0951-8320. DOI: 10.1016/j.ress.2019.106550.

[36] J. D. Sørensen and H. S. Toft, "Safety factors – IEC 61400-1, ed.4: Background document," Department of Wind Energy, Technical University of Denmark, DTU Wind Energy E 2014(0066EN), 2014. [Online]. Available: https://vbn.aau.dk/ws/portalfiles/portal/559225421/Safety_Factors_IEC_61400-1_ed_4_-_background_document.pdf.

[37] J.M.J. Journée and W.W. Massie, *Offshore Hydrodynamics*, First Edition. Delft University of Technology, Jan. 2001.

[38] J. R. Morison, J. W. Johnson, and S. A. Schaaf, "The force exerted by surface waves on piles," *Journal of Petroleum Technology*, vol. 2, no. 5, pp. 149–154, May 1950, ISSN: 0149-2136. DOI: 10.2118/950149-G.

[39] R. C. MacCamy and R. A. Fuchs, "Wave forces on piles: A diffraction theory," U.S. Army Corps of Engineers, Beach Erosion Board, Washington, D.C., USA, Technical Memorandum No. 69, 1954.

[40] J. Velarde, C. Kramhøft, J. D. Sørensen, and G. Zorzi, "Fatigue reliability of large monopiles for offshore wind turbines," *International Journal of Fatigue*, vol. 134, p. 105 487, May 2020. DOI: 10.1016/j.ijfatigue.2020.105487.

[41] I. Mosquera-Mosquera, M. L. Simão, P. M. Videiro, and L. V. Sagrilo, "Evaluating the impact of climate change on offshore structures design: A practical case study," *Applied Ocean Research*, vol. 94, p. 101 992, Jan. 2020, ISSN: 0141-1187. DOI: 10.1016/j.apor.2019.101992.

[42] L. E. Borgman, "Ocean wave simulation for engineering design," *Journal of the Waterways and Harbors Division*, vol. 93, no. 4, pp. 1–26, Nov. 1967.

[43] L. Ziegler, "Probabilistic estimation of fatigue loads on monopile-based offshore wind turbines," M.S. thesis, TU Delft and NTNU, May 2015.

[44] M. Kühn, "Dynamics and design optimisation of offshore wind energy conversion systems," Ph.D. dissertation, DUWIND, Delft University Wind Energy Research Institute, 2001, 282 pp.

[45] A. K. Rajeevan, P. V. Shouri, and U. Nair, "Markov modeling and reliability allocation in wind turbine for availability enhancement," *Life Cycle Reliability and Safety Engineering*, vol. 7, no. 3, pp. 147–157, Sep. 2018, ISSN: 2520-1352, 2520-1360. DOI: 10.1007/s41872-018-0054-8.

[46] S. Faulstich, B. Hahn, and P. J. Tavner, "Wind turbine downtime and its importance for offshore deployment," *Wind Energy*, vol. 14, no. 3, pp. 327–337, Apr. 2011. DOI: 10.1002/we.421.

[47] R. P. Brent, "An algorithm with guaranteed convergence for finding a zero of a function," *The Computer Journal*, vol. 14, no. 4, pp. 422–425, 1971. DOI: 10.1093/comjnl/14.4.422.

[48] M. Casas-Prat, M. A. Hemer, G. Dodet, J. Morim, X. L. Wang, N. Mori, I. Young, L. Erikson, B. Kamranzad, P. Kumar, M. Menéndez, and Y. Feng, "Wind–wave climate changes and their impacts," *Nature Reviews Earth & Environment*, vol. 5, pp. 23–42, 2024. DOI: 10.1038/s43017-023-00502-0.

[49] D.-V. Ngo, Y.-S. Chun, and D.-H. Kim, "Long-term fatigue damage assessment of a 22 MW offshore wind turbine considering climate change scenarios," *Structures*, vol. 302, p. 110 182, 2025. DOI: 10.1016/j.istruc.2025.110182.

[50] J.-T. Horn, J. R. Krokstad, and B. J. Leira, “Impact of model uncertainties on the fatigue reliability of offshore wind turbines,” *Marine Structures*, vol. 64, pp. 174–185, 2019. DOI: 10.1016/j.marstruc.2018.11.004.

Appendices

A. Acknowledgement on the Usage of AI

During the work carried out for this thesis, OpenAI's ChatGPT was used to support in various tasks. These tasks included:

- Writing plotting functions to plot results.
- Code optimisation and debugging.
- Assisting with spelling and grammar correction.
- Enhancing clarity and coherence of the text.

All outputs of ChatGPT were carefully reviewed. AI tools were not used in the generation of scientific arguments or interpretation of results. The responsibility for the accuracy, originality and academic integrity of the thesis rests with the author.

B. Description of Metocean Climate

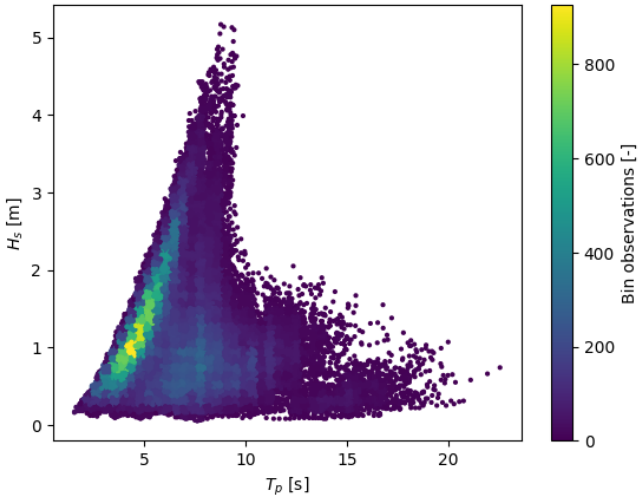

Figure 1: H_s-T_p scatterplot with amount of observations per H_s-T_p bin indicated, a total of 50 linearly spaced bins were used for both H_s as T_p.

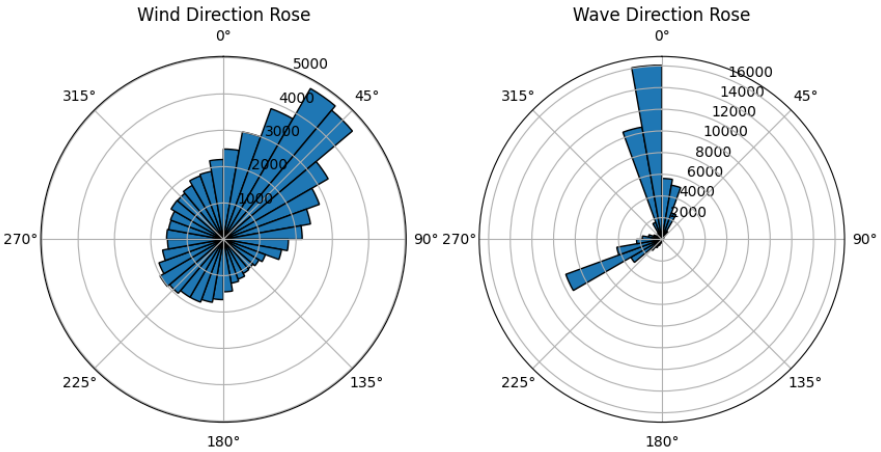

Figure 2: Wind and wave rose direction plot, with both directions indicating direction where wind or waves were coming from.

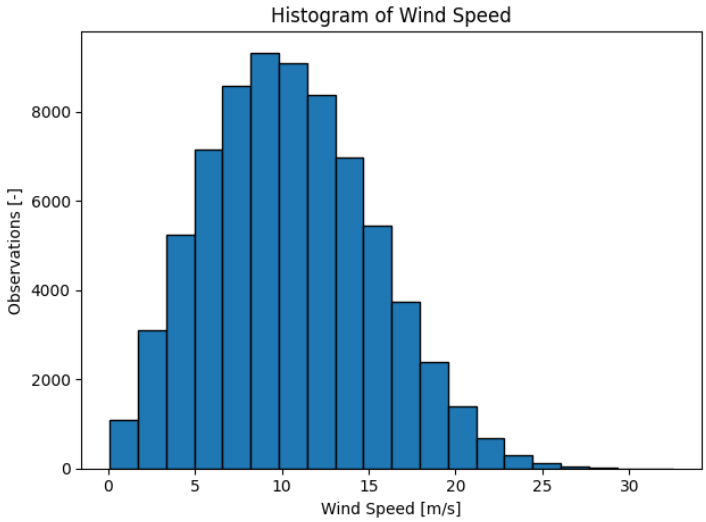

Figure 3: Wind speed Histogram of wind speed at height of 116 m.

C. Results of Calibration of Availability Model across Six Sectors

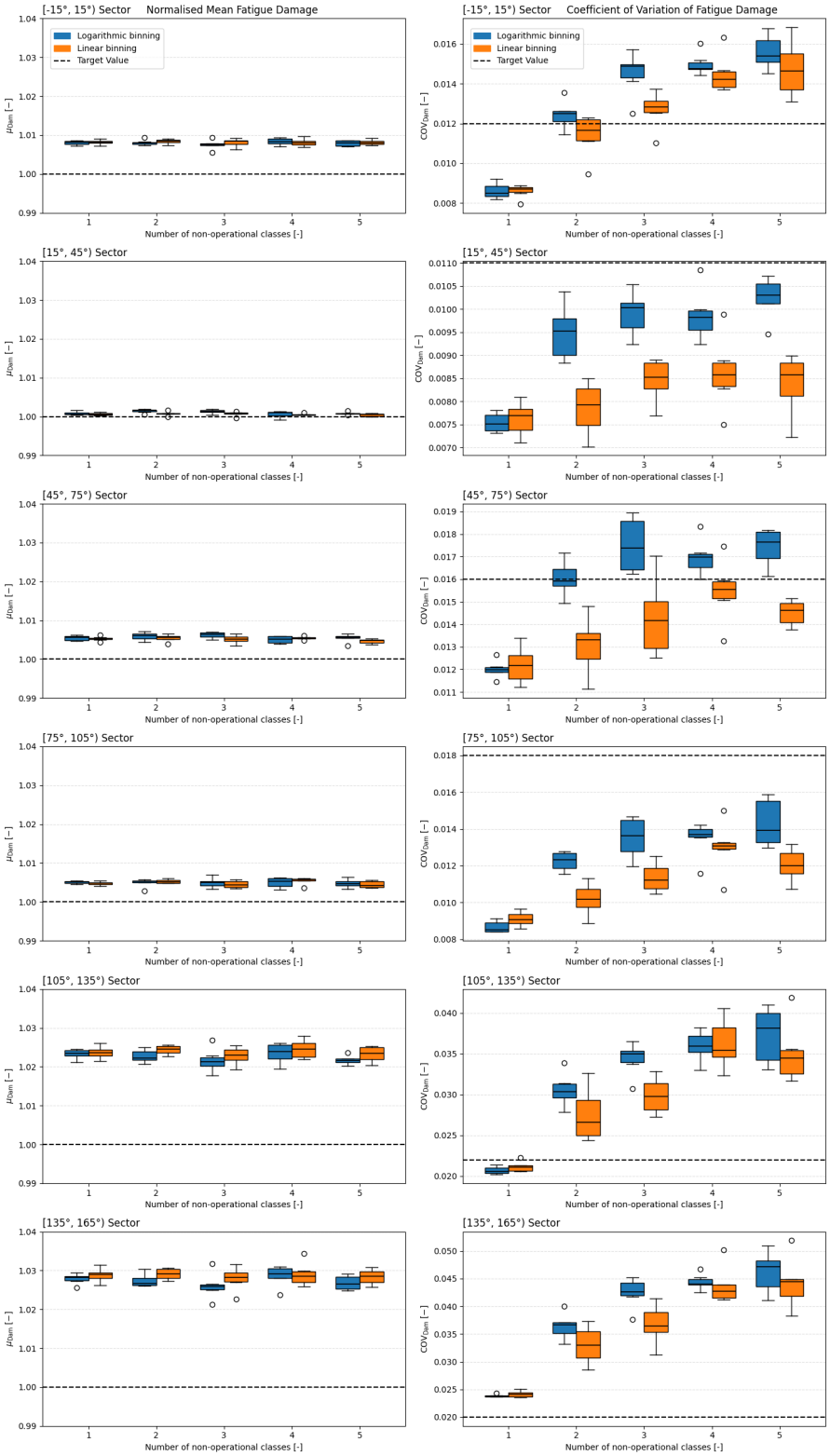

Figure 4: Influence of different numbers of non-operational classes and binning strategies on mean fatigue damage and fatigue damage COV across 6 seeds for all sectors.

D. Final Model Performance across Six Sectors

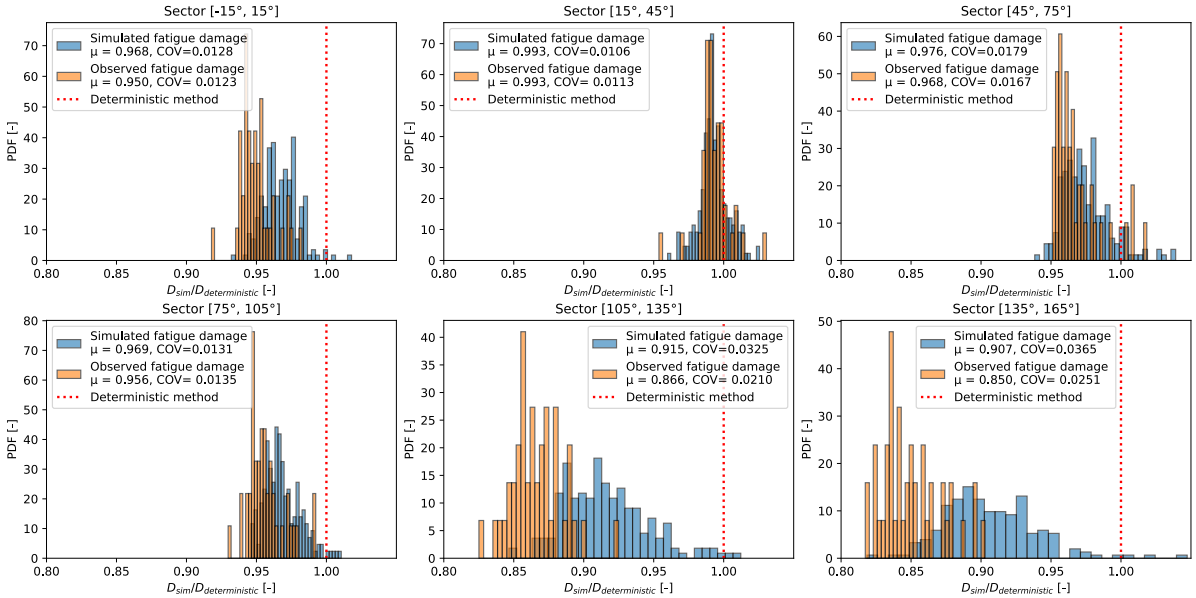

Figure 5: Comparison between final model and observed fatigue damage variance across all sectors. Both histograms are normalized such that the area equals one, representing empirical estimates of the PDF.

E. Results of Full Design Life Fatigue Damage Simulation across Six Sectors

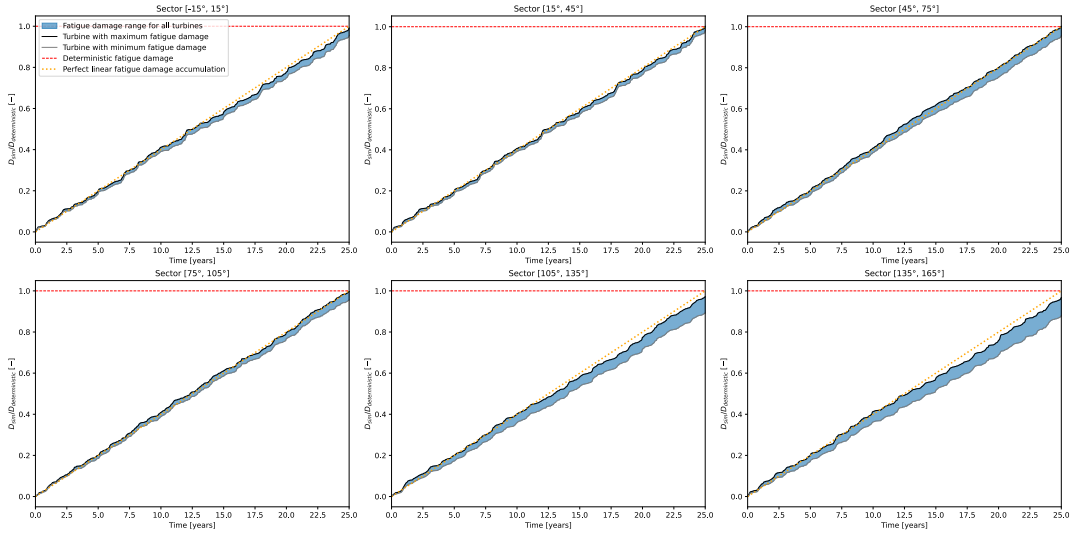

(a) Fatigue damage accumulation for all sectors with the turbine with maximum and minimum fatigue damage indicated, the dashed red line is the deterministic reference level, and the orange dotted line shows perfect linear accumulation.

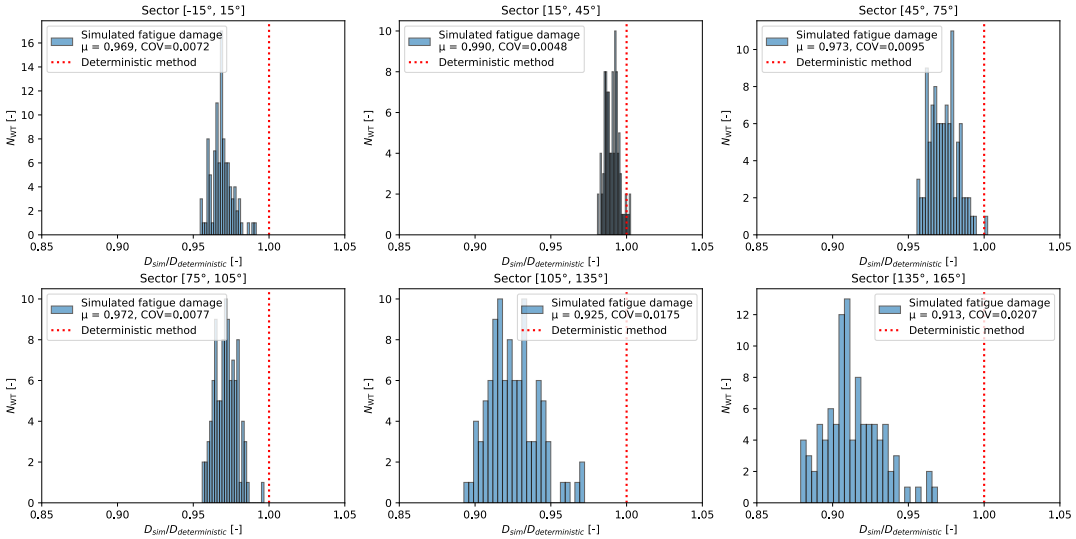

(b) Histogram of the normalised fatigue damage after the 25-year design life for all turbines, for every sector. The vertical dashed red line marks the deterministic reference level.

Figure 6: Predicted fatigue damage for the 8 MW turbine for all sectors. Figure (a) shows the damage accumulation over the 25-year design life. Figure (b) shows the distribution of the resulting fatigue damage at the end of the design. Fatigue damage values are normalised against the deterministic (90% operational / 10% non-operational) method recommended by DNV.

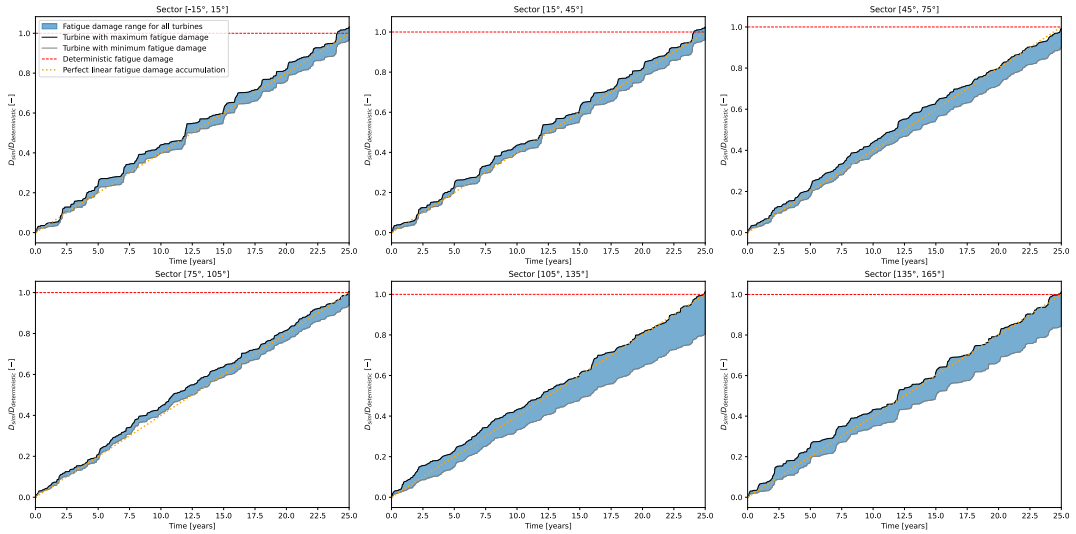

(a) Fatigue damage accumulation for all sectors with the turbine with maximum and minimum fatigue damage indicated, the dashed red line is the deterministic reference level, and the orange dotted line shows perfect linear accumulation.

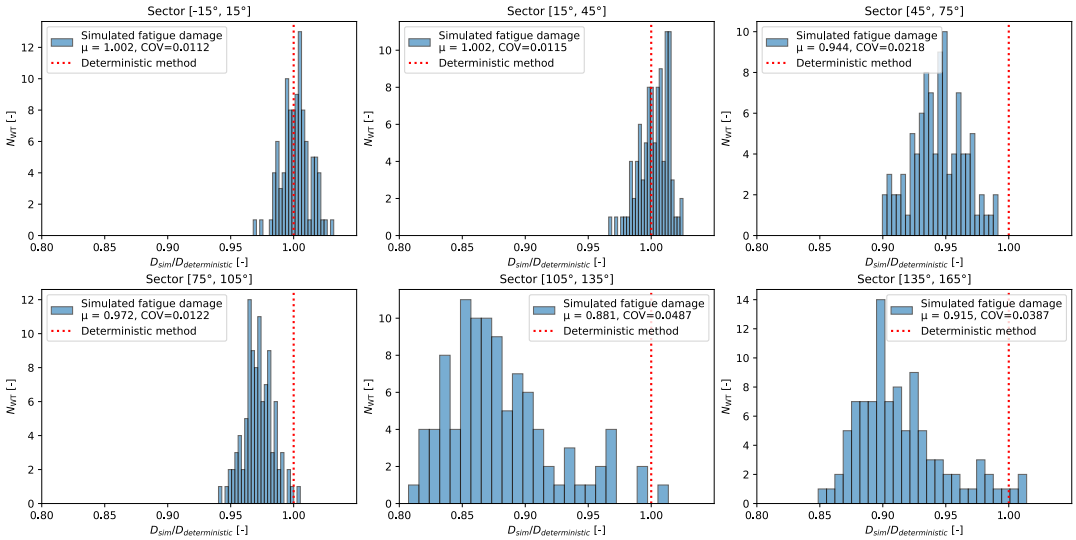

(b) Histogram of the normalised fatigue damage after the full 25-year life for all turbines, for every sector. The vertical dashed red line marks the deterministic reference level.

Figure 7: Predicted fatigue damage for the 14 MW turbine for all sectors. Figure (a) shows the damage accumulation over the 25-year design life. Figure (b) shows the distribution of the resulting fatigue damage at the end of the design. Fatigue damage values are normalised against the deterministic (90% operational / 10% non-operational) method recommended by DNV.

F. Results of Full Design Life Fatigue Damage Simulation across Six Sectors with Different Unavailability Ratio

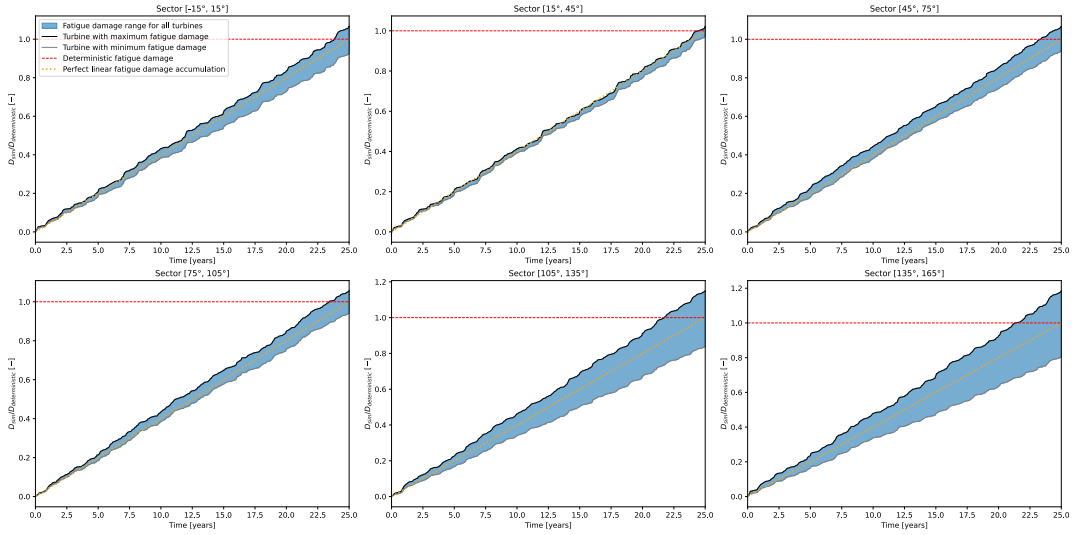

(a) Time evolution (0–25 years) of accumulated fatigue damage considering *all* wind-direction sectors. with the turbine with maximum and minimum fatigue damage indicated, the dashed red line is the deterministic reference level, and the orange dotted line shows perfect linear accumulation.

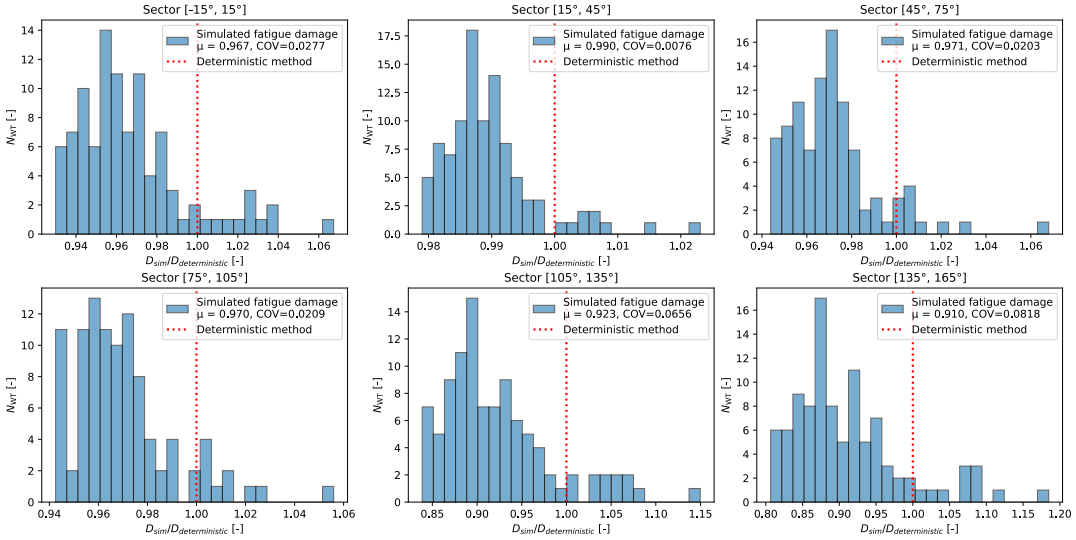

(b) Histogram of the normalised fatigue damage after the full 25-year life for all turbines, aggregated over every sector. The vertical dashed red line marks the deterministic reference level. Please note that the X-axis is not the same for each sector

Figure 8: Predicted fatigue damage for the 8 MW turbine for all sectors, when the unavailability ratio is not bounded between 4% and 10%. Figure (a) fatigue damage accumulation over the 25-year design life. Figure (b) Distribution of the resulting fatigue damage at the end of design life. All values are normalised with respect to the recommended 90% operational / 10% non-operational practice of DNV.

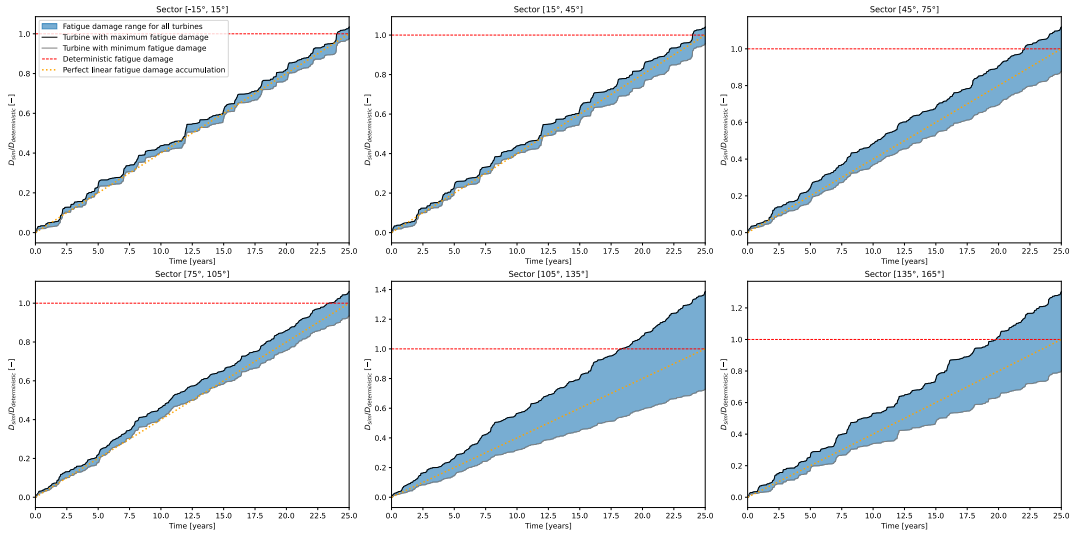

(a) Time evolution (0–25 years) of accumulated fatigue damage considering *all* wind-direction sectors. with the turbine with maximum and minimum fatigue damage indicated, the dashed red line is the deterministic reference level, and the orange dotted line shows perfect linear fatigue damage accumulation.

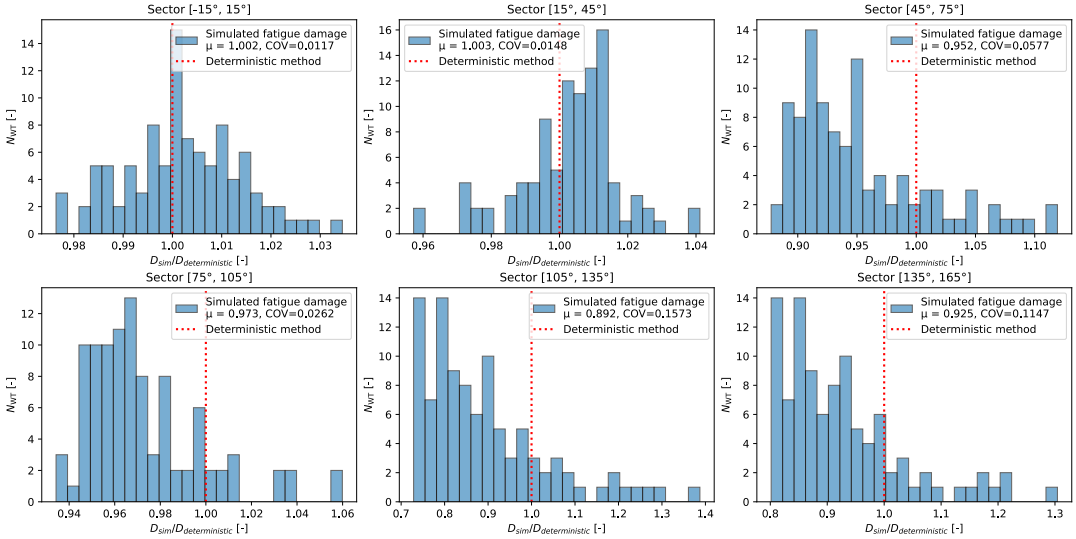

(b) Histogram of the normalised fatigue damage after the full 25-year life for all turbines, aggregated over every sector. The vertical dashed red line marks the deterministic reference level. Please note that the X-axis is not the same for each sector.

Figure 9: Predicted fatigue damage for the 14 MW turbine for all sectors, when the unavailability ratio is not bounded between 4% and 10%. Figure (a) fatigue damage accumulation over the 25-year design life. Figure (b) Distribution of the resulting fatigue damage at the end of design life. All values are normalised with respect to the fatigue damage obtained by following the recommended 90% operational / 10% non-operational practice of DNV.